

Semiclassical Theory of Quantum Chaotic Transport: Phase-Space Splitting, Coherent Backscattering and Weak Localization

Ph. Jacquod^{1,2} and Robert S. Whitney^{2,3}

¹ *Department of Physics, University of Arizona, 1118 E. 4th Street, Tucson, AZ 85721, USA*

² *Département de Physique Théorique, Université de Genève, 1211 Genève 4, Switzerland*

³ *Institut Laue-Langevin, 6 rue Jules Horowitz, B.P. 156, 38042 Grenoble, France*

(Dated: May 10, 2006)

We investigate transport properties of quantized chaotic systems in the short wavelength limit. We focus on non-coherent quantities such as the Drude conductance, its sample-to-sample fluctuations, shot-noise and the transmission spectrum, as well as coherent effects such as weak localization. We show how these properties are influenced by the emergence of the Ehrenfest time scale τ_E . Expressed in an optimal phase-space basis, the scattering matrix acquires a block-diagonal form as τ_E increases, reflecting the splitting of the system into two cavities in parallel, a classical deterministic cavity (with all transmission eigenvalues either 0 or 1) and a quantum mechanical stochastic cavity. This results in the suppression of the Fano factor for shot-noise and the deviation of sample-to-sample conductance fluctuations from their universal value. We further present a semiclassical theory for weak localization which captures non-ergodic phase-space structures and preserves the unitarity of the theory. Contrarily to our previous claim [Phys. Rev. Lett. **94**, 116801 (2005)], we find that the leading off-diagonal contribution to the conductance leads to the exponential suppression of the coherent backscattering peak and of weak localization at finite τ_E . This latter finding is substantiated by numerical magnetoconductance calculations.

PACS numbers: 73.23.-b, 74.40.+k, 05.45.Mt, 05.45.Pq

I. INTRODUCTION

Closed chaotic systems are classically characterized by ergodicity, mixing and a positive Kolmogorov-Sinai (KS) entropy [1]. These three characteristics form a hierarchy: mixing systems are ergodic, and systems with positive KS entropy are mixing, but the reverse is not necessarily true. Ergodicity means that phase-space averages equal time averages, while the definition of both mixing and KS entropy requires the introduction of some phase-space coarse-graining. For mixing, one needs to define finite-sized phase-space cells inside which points originating from two initially well separated distributions of initial conditions are equally likely to be found. As time goes by, mixing occurs on smaller and smaller scales, i.e. the minimal volume of these cells decreases. The KS entropy is defined from the measure of the intersection of the cells with their back evolution under the system dynamics. A positive KS entropy means an exponential production of information, and thus the generation of randomness in the Kolmogorov sense, as more and more different trajectories emerge from apparently indistinguishable initial conditions [1]. For closed systems, the KS entropy is related to the exponential sensitivity to initial conditions, and equals the sum of the associated positive Lyapunov exponents [1, 2].

The situation becomes different once the system is open and scattering trajectories are considered. Phase-space structures emerge then which are prohibited by ergodicity and mixing, even in systems which have a positive KS entropy when closed. These structures and their influence on quantum transport are the focus of this article. We will see how their occurrence affects transport

through open quantized chaotic systems in the semiclassical, short wavelength limit. They result in a splitting of the cavity into two cavities in parallel, one where transport is ruled by classical determinism and one where transport exhibits quantum stochasticity.

A. Classical chaos in open systems

We specialize to two-dimensional chaotic cavities in a two-terminal geometry. Typical nonergodic structures occurring in such open chaotic systems are illustrated in Fig. 1. A color plot of the transmission probability is shown on a phase-space projection of one of the two openings. The horizontal axis gives the position on a cross-section of the opening, normalized by the cavity perimeter L , and the vertical axis gives the momentum component of injection into the system, parallel to the cavity boundary, and normalized by the Fermi momentum p_F . Both the real-space set-up and the dimensionless phase-space we use are defined in Fig. 2.

Band-like structures such as those appearing in Fig. 1 have been reported and discussed earlier [3, 4, 5, 6, 7, 8]. All scattering trajectories whose initial point lies in one of the bands have approximately the same dwell time through the system [9]. The typical dwell time τ of a band determines its width as $\simeq (W/L) \exp[-\lambda\tau]$ [4] (W is the width of the opening and λ is the Lyapunov exponent). Thus the largest blue and red bands in Fig. 1 respectively correspond to direct reflection and transmission, while thinner bands correspond to longer dwell times through the system. Trajectories inside a band are transported in one bunch, and the phase-space volume

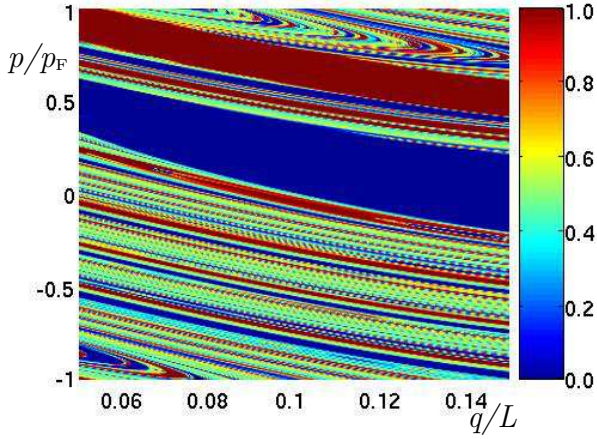


FIG. 1: (Color online) Classical phase-space color plot of the transmission probability from the phase-space projection of the injection lead (see Fig. 2). The phase-space has been coarse-grained by a rectangular grid with $9 \cdot 10^4$ cells, and the transmission probability in each cell has been calculated by time-evolving 10^4 classical trajectories per cell. Higher transmissions correspond to red, lower transmissions to blue. The dynamical system used is the open kicked rotator as defined in Section VI.

they occupy is blocked for other trajectories by Liouville's theorem. Because trajectories remain inside the system for a finite time, the definition of ergodicity, that

$$\Omega^{-1} \int_{\Omega} d\mathbf{p} d\mathbf{q} f(\mathbf{p}, \mathbf{q}; t) = \lim_{\tau \rightarrow \infty} \tau^{-1} \int_0^{\tau} dt f(\mathbf{p}_0, \mathbf{q}_0; t), \quad (1)$$

for almost all functions $f(\mathbf{p}, \mathbf{q}; t)$ and almost all phase-space points $(\mathbf{p}_0, \mathbf{q}_0) \in \Omega$ no longer holds, but depends on $(\mathbf{p}_0, \mathbf{q}_0)$. The time-integral on the right-hand side of Eq. (1) extends only up to the dwell time t_0 of the one trajectory going through $(\mathbf{p}_0, \mathbf{q}_0)$, and accordingly Eq. (1) cannot be preserved over the full phase-space Ω . Simultaneously, mixing occurs on a given scale only for the subset of trajectories longer than some finite dwell time. Scattering trajectories through open systems have a continuous distribution of dwell times $P(t)$ and because of the exponentially decreasing volume of scattering bands, mixing occurs on exponentially smaller scales on longer trajectories. Reversing the argument, a given phase-space resolution volume ξ corresponds to a time scale $\tau_{\xi} \approx \lambda^{-1} \ln[(W/L)^2/\xi]$. Long trajectories with $\tau > \tau_{\xi}$ exhibit mixing on the scale ξ , while short trajectories with $\tau < \tau_{\xi}$ lie on bands well resolved by ξ -cells, which therefore do not have the mixing property. These two sets of classical scattering trajectories have no phase-space overlap.

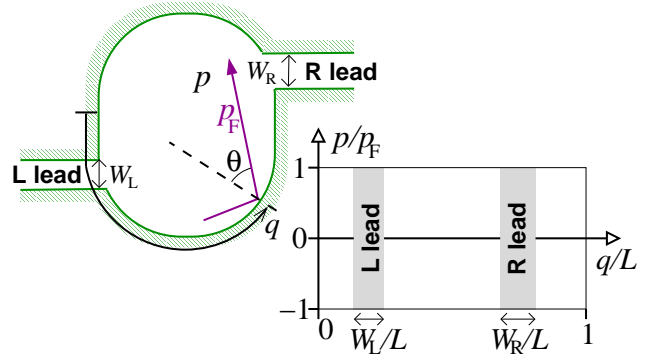


FIG. 2: (Color online) Sketch of a two-terminal open chaotic cavity (top left) and its phase-space represented as a Poincaré surface of section on the boundary of the cavity (bottom right). All momenta on the energy surface ($E = p_F^2/2m$) are parametrized by the tangential momentum p running from $-p_F$ to p_F . All possible positions on the boundary are parametrized by q running from zero to L , where L is the circumference of the cavity. The phase-space is made dimensionless by normalizing momenta and real-space coordinates with p_F and L respectively.

B. Quantum chaos in open systems

A finite resolution scale emerges naturally when the system is quantized: the phase-space becomes tiled with cells of volume $2\pi\hbar$. For particles with a finite Fermi wavelength λ_F , this is equivalent to tiling the dimensionless phase-space projection of the leads (see Fig. 2) with cells of volume $\hbar_{\text{eff}} = \lambda_F/L$, the effective Planck's constant. This leads to the existence of a finite number $N = \text{Int}[2W/\lambda_F]$ of conduction channels through the system. As \hbar_{eff} is made smaller and smaller, all classical parameters being kept constant (the semiclassical limit), more and more of the band structures of Fig. 1 are resolved (see Fig. 3). Conversely, more and more of the conduction channels are supported by one and only one classical transmission or reflection band, and thereby become deterministic. It is thus natural to investigate the effect that the lack of mixing of short trajectories has on properties of open quantum chaotic systems.

Transport through ballistic quantum cavities, so-called quantum dots, has been investigated intensively in recent years [10]. In the regime where the dot's size is much larger than the Fermi wavelength, $L \gg \lambda_F$, transport has been shown to depend on the integrability or lack thereof of the classical dynamics, as determined by the confinement potential [11, 12]. Most experimental investigations so far have focused on the limit of few, $\lesssim 10$ conduction channels, where it has been found that quantum transport in the chaotic case exhibits a universality which is well captured by the Random Matrix Theory (RMT) of transport [13, 14]. Recently, a semiclassical theory for the conductance of ballistic cavities has been developed [15], confirming the common belief that RMT

universality applies at least to a certain regime of ballistic chaos.

It is however well-known that physically relevant time scales restrict the range of validity of RMT. In recent years it has become clear that the *Ehrenfest* time τ_E does this in ballistic quantum chaotic systems, with RMT ceasing to be valid when τ_E becomes relevant. The Ehrenfest time is the time it takes for the chaotic classical dynamics to stretch a narrow wave packet, of spatial extension λ_F , to some relevant classical length scale \mathcal{L} . Since the stretching is exponential in a chaotic system, one has $\tau_E = \lambda^{-1} \ln[\mathcal{L}/\hbar_{\text{eff}} L]$ [16]. The scattering of an initially localized wavepacket into all possible modes (similar to *s*-wave scattering on a restricted portion of phase-space) is only established after classical mixing has set in on the scale \hbar_{eff} , i.e. for times longer than τ_E . For shorter times, the quantum dynamics is deterministic. One thus expects deviations from RMT to emerge as τ_E/τ_D increases.

This line of reasoning has been qualitatively confirmed in the cavity transport experiments of Ref. [17], which observed a significant reduction of the electronic shot-noise power below its RMT value upon opening the cavity more and more. This reduction is very likely due to an increasing fraction of deterministic channels in the transmission spectrum of the cavity which can be understood as follows. The shot-noise power (the intrinsically quantum part of the fluctuations of the electronic current) is usually quantified by the dimensionless Fano factor F , the ratio of the shot-noise to the Poissonian noise [18], which can be expressed in term of the transmission spectrum $T_i \in [0, 1]$ of the cavity as [18]

$$F = \sum_i T_i(1 - T_i) / \sum_i T_i. \quad (2)$$

Hence deterministic channels, those having $T_i = 0$ or 1 , do not contribute to F . Such channels appear as the classical bands discussed above are quantum mechanically resolved, which can be achieved either by reducing the dwell time or by reducing the Fermi wavelength. The former change was more appropriate for the experimental set-up of Ref. [17], and the latter change is illustrated in the numerics of Fig. 3. We show three quantum phase-space plots for a fixed classical set-up (the same as for Fig. 1). Plotted is the quantum transmission probability $\langle(x, p)|\mathbf{T}|(x, p)\rangle$ for a fixed grid of initial coherent states $|(x, p)\rangle$, i.e. isotropic Gaussian wavepackets centered on (x, p) . The three panels from left to right correspond to smaller and smaller λ_F . It is seen that as λ_F decreases, finer and finer phase-space structures are resolved. Moreover, coherent states entirely lying on deep red (deep blue) regions have $\langle(x, p)|\mathbf{T}|(x, p)\rangle = 1$ (0), and are therefore eigenstates of \mathbf{T} . Any of them can carry a quantum channel which does not contribute to shot-noise (the total number of deterministic channels is obtained only after the orthogonalization of the coherent states, see below). With decreasing λ_F , the number of deterministically transmitted coherent states increases faster

than the total number of channels, inducing the reduction of the shot-noise power below its RMT value.

The suppression of the Fano factor in the semiclassical limit was anticipated long ago [19]. More recent works quantitatively predicted a suppression $F \propto \exp(-\tau_E/\tau_D)$, in term of the new Ehrenfest time scale and the average dwell time τ_D through the system [20, 21], a suppression which was related to the phase-space resolution picture of Ref. [4] given above and confirmed numerically in Refs. [5, 7]. Ref. [22] presented a phase-space semiclassical approach resolving the classical bands which showed that the fraction of deterministic transmission eigenvalues not contributing to noise is $\propto [1 - \exp(-\tau_E/\tau_D)]$. Following the numerous recent investigations of the quantum-to-classical correspondence in open systems, which we now proceed to briefly summarize, it has become clear that $\tau_E/\tau_D \rightarrow 0$ is a necessary condition for complete RMT universality [23]. As is illustrated in Fig. 4, this condition is never satisfied in the semiclassical limit $\hbar_{\text{eff}} \rightarrow 0$.

Following Ref. [24] which suggested that the existence of a finite τ_E discriminates quantum chaotic from quantum disordered systems (with the former class exhibiting deviations from universality), many investigations have been devoted to the study of open quantum chaotic systems at finite τ_E [23]. Focusing on transport, it is by now well established numerically that, as $\tau_E/\tau_D \rightarrow \infty$, the Fano factor disappears [5], and sample-to-sample conductance fluctuations lose their universality. Simultaneously, parametric conductance fluctuations appear to remain universal [6, 7]. The weak localization correction to the conductance was first predicted to disappear exponentially as $\delta g \propto \exp[-2\tau_E/\tau_D]$ [24] or $\delta g \propto \exp[-\tau_E/\tau_D]$ [25]. Early numerical works, on the other hand, concluded that δg is independent of τ_E/τ_D [26]. This puzzle was resolved in Ref. [27] (though some skepticism remained, on the part of the authors of the present article amongst others) whose analytical approach predicted $\delta g \propto \exp[-\tau_E/\tau_D]$ in agreement with numerical simulations. Below we will present both an analytical, semiclassical treatment of weak localization with a special emphasis on backscattering and unitarity, and numerical magnetoconductance data giving a microscopic confirmation of the conclusion $\delta g \propto \exp[-\tau_E/\tau_D]$ of Ref. [27].

There are currently several theories for open quantum chaotic systems at finite τ_E . First, the stochastic quasiclassical theory mimics the post-Ehrenfest time mode-mixing by introducing fictitious random scatterers with a scattering rate appropriately tuned [20, 24, 27]. It is developed from standard methods in disordered systems, but breaks time-reversal symmetry at the classical level already. Second, there is a semiclassical theory [25], which until now had not been shown to preserve the unitarity of the scattering matrix (and hence conserve the current). Third, a phenomenological model originating from Ref. [4] models the total electronic fluid as two coexisting phases, a classical and a quantum one. At this level, the theory is referred to as the two-phase

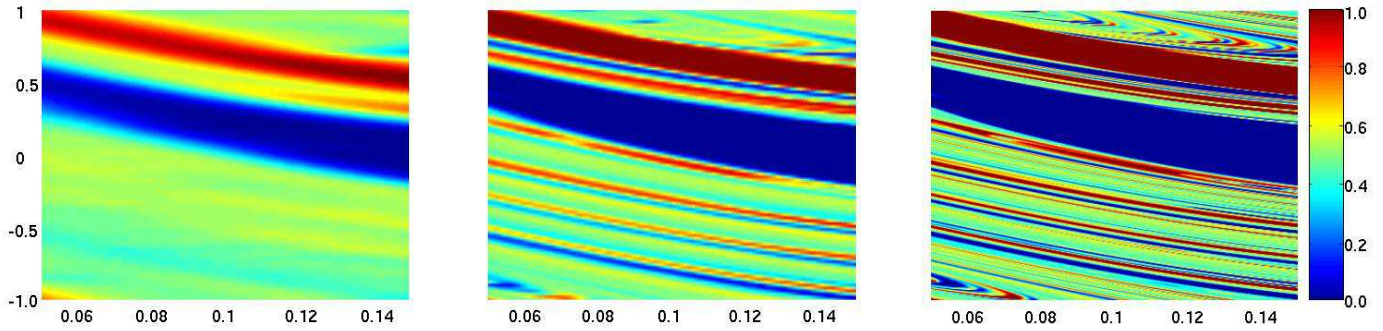


FIG. 3: (Color online) Quantum phase-space color plots of the transmission probability from the injection lead. The system is the quantum equivalent of the classical system of Fig. 1. The phase-space has been coarse-grained by a rectangular grid with $9 \cdot 10^4$ points. Starting from each point of the grid, an isotropic Gaussian wave-packet has been time-evolved and its transmission probability calculated. From left to right, the three panels correspond to decreasing effective Planck's constant $\hbar_{\text{eff}} = 2\pi/M$ with $M = 512$ (with a conductance $g = 22.4$ and a Fano factor $F = 0.193$), 8192 ($g = 375.9$ and $F = 0.121$) and 131072 ($g = 5990.8$ and $F \approx 0.08$) respectively. More and more fine-structured details of the classical phase-space are resolved as $\hbar_{\text{eff}} \rightarrow 0$. Higher transmissions correspond to red, lower transmissions to blue color.

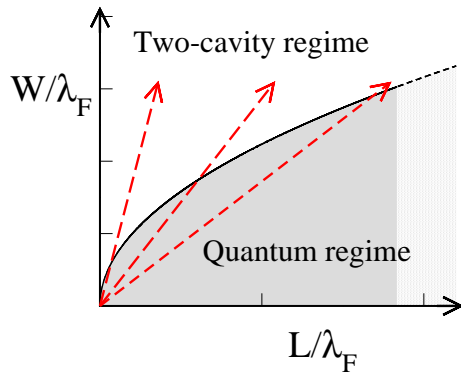


FIG. 4: (Color online) Schematic of the different transport regimes through a ballistic chaotic cavity with perimeter L coupled to leads of width W . Above the separatrix, the system splits into two effective cavities, one purely classical and the other quantum mechanical. Only the latter contains quantum effects such as non-deterministic transmission and quantum interferences. Below the separatrix $W = (\lambda_F L)^{1/2}$ (solid curve), all modes are quantum mechanical (grey area). The red dashed arrows indicate the semiclassical limit of $\hbar_{\text{eff}} \rightarrow 0$ at fixed classical parameters. The slope of the arrows is given by the inverse dwell time τ_D .

fluid model [7, 22]. With the additional surmise made in Ref. [4] that the quantum phase has RMT properties, one gets the effective RMT model. The effective RMT model successfully explains the behavior of shot-noise, the transmission spectrum and conductance fluctuations, but is in contradiction with the disappearance of weak localization [27]. The suppression of weak localization at large τ_E/τ_D invalidates the effective RMT model, but not the two-phase fluid model, as we will explicitly see below.

C. Outline of this article

In this article, we focus on quantities such as the average conductance, shot-noise and the transmission spectrum in ballistic chaotic cavities, as well as the weak localization correction to the conductance as $\hbar_{\text{eff}} \rightarrow 0$. These quantities are strongly influenced by the emergence of the open cavity Ehrenfest time $\tau_E^{\text{op}} = \lambda^{-1} \ln[(W/L)^2/2\pi\hbar_{\text{eff}}]$ [28]. All classical parameters being fixed, that limit inevitably turns any system into a nonuniversal quantum chaotic one as τ_E^{op} becomes finite (see Fig. 4). We calculate the scattering matrix in a basis that optimally resolves phase-space structures and show that the system splits into two cavities in parallel. This provides a foundation for the two-phase fluid model. We go significantly beyond our previous work, Ref. [22], with (i) a detailed construction of a basis which optimally resolves those phase-space structures and (ii) an explicit semiclassical calculation of the weak localization correction to the conductance which preserves the unitarity of the scattering matrix to leading order.

The outline of the paper goes as follows. In Section II, we discuss the nonergodic classical structures of open chaotic systems such as those shown in Fig. 1 and the Ehrenfest time scale that accompanies them. Our task requires that we resolve quantum mechanically these classical phase-space structures. This suggests that we employ a semiclassical theory. The existing such theories [11, 15] have to be replaced by a phase-space resolving theory, which requires the construction of an appropriate orthogonal mode basis. This is done in Section III. We then write the system's scattering matrix in this basis, and show how this results in phase-space splitting at the quantum level in Section IV. Amplifying on that, we show how deterministic modes emerge and calculate the average Drude conductance and its sample-to-sample

fluctuations at large τ_E^{op} . In Section V, we present our semiclassical theory for the weak localization correction to the conductance. Several key aspects absent in previous semiclassical treatments are stressed here. In particular we present the first semiclassical calculation of the coherent backscattering peak at finite $\tau_E^{\text{op}}/\tau_D$. We show that both coherent backscattering and weak localization are exponentially suppressed $\propto \exp[-\tau_E^{\text{cl}}/\tau_D]$ with the closed cavity Ehrenfest time $\tau_E^{\text{cl}} = \lambda^{-1} \ln[\hbar_{\text{eff}}^{-1}]$. This is so, because weak localization and coherent backscattering come from trajectories longer than $\tau_E^{\text{op}} + \tau_E^{\text{cl}}$, which have an exponentially small relative weight $\exp[-\tau_E^{\text{cl}}/\tau_D]$ in the stochastic block of the scattering matrix. The existence of two separated fluids is however confirmed. We demonstrate that the classical phase-space structures (which give rise to phase-space splitting) must be included in the semiclassical treatment to preserve the unitarity of the scattering matrix at nonvanishing value of $\tau_E^{\text{op}}/\tau_D$. We also point out the origin of the discrepancy between our final conclusion, that $\delta g \propto \exp[-\tau_E^{\text{cl}}/\tau_D]$, and our earlier claim that δg remains at its universal value in the deep semiclassical limit [22]. We finally present numerical magnetoconductance data confirming our theory. Summary and conclusions are presented in Section VII, and technical details discussed in the Appendices.

II. CLASSICAL SCATTERING STRUCTURES AND EHRENFEST TIMES

A. Transmission and reflection bands

We consider classical scattering trajectories. They are injected into the cavity from one of the two leads, say the left (L) lead, with initial position q and momentum p on a cross-section of the lead. The momentum is on the Fermi energy surface $E = p_F^2/2m$. The trajectory is determined by ballistic motion inside the confinement potential defining the cavity, until the particle hits the boundary between the cavity and one of the leads, at what time it escapes. Throughout this paper we will consider perfectly transparent leads.

Scattering trajectories are not isolated, instead they occur in bands (see Fig. 1). As mentioned in the introduction, a scattering band is a phase-space structure occurring in open systems, even when their closed counterpart is fully chaotic. It contains a set of trajectories which exit at approximately the same time through the same lead [9], having followed similar trajectories through the cavity, in the sense that any trajectory in the band can be topologically deformed into any other. The situation is sketched in Fig. 5. Bands on the injection lead are defined by the overlap of that lead with the time-reversed evolution of the exit lead, including absorption at both leads.

For an individual system, the exact number and area of the bands depends on the specifics of the lead positions

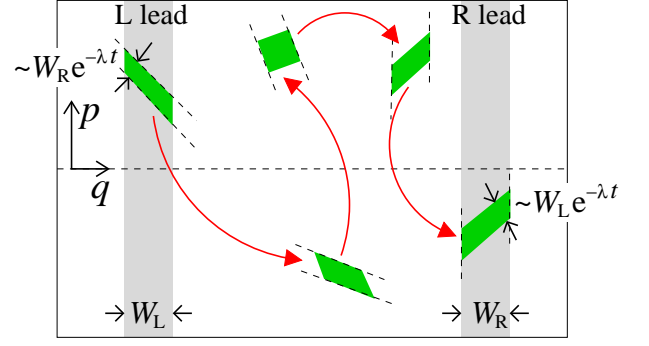


FIG. 5: (Color online) Time evolution of an L to R transmission band (parallelograms) on the boundary of the cavity of Fig. 2. The leads are indicated by the shaded rectangles.

and widths, and the cavity shape. However, averaged properties calculated over an ensemble of cavities with the same dwell time and Lyapunov exponent can be calculated. The asymptotic average survival probability is exponential [29],

$$\rho(\tau) = \exp[-\tau/\tau_D]. \quad (3)$$

It depends solely on the average dwell time τ_D given by

$$\tau_D = \frac{\pi A}{v_F(W_L + W_R)}. \quad (4)$$

Here A is the area of the cavity and we considered leads with different widths $W_{L,R}$.

In the dimensionless phase-space defined in Fig. 2, where momenta and distances are measured in units of p_F and L respectively, the injection lead (we always assume this is the L lead) has a dimensionless phase-space area of

$$\Sigma_L = 2W_L/L. \quad (5)$$

The fraction of the lead phase-space which couples to transmitting trajectories is $\sim W_R/(W_L + W_R)$, with the rest coupling to reflecting trajectories. The average phase-space area of a single transmission (L→R) or reflection (L→L) band which exits at time τ , is given by

$$\langle \Sigma_{L \rightarrow K}(\tau) \rangle \sim \frac{W_L W_K}{L^2} e^{-\lambda \tau}, \quad (6)$$

where $K = L, R$. The average number $\langle n_{L \rightarrow K}(\tau) \rangle$ of bands exiting at time τ through lead K is given by multiplying $\Sigma_L/\langle \Sigma_{L \rightarrow K}(\tau) \rangle$ by the probability $(W_K/L) \exp[-\tau/\tau_D]$ to escape through the K lead at τ . Hence one has

$$\langle n_{L \rightarrow L}(\tau) \rangle = \langle n_{L \rightarrow R}(\tau) \rangle \sim \exp[\lambda \tau (1 - (\lambda \tau_D)^{-1})]. \quad (7)$$

Since we assume fully developed chaos, $\lambda \tau_D \gg 1$, we see that the average number of bands diverges as τ goes to infinity even though the sum of their phase-space areas goes to zero. We also note that the average number of reflection and transmission bands are equal, with only their areas being dependent on $W_{L,R}$.

B. Ehrenfest times and modes on classical bands

The Ehrenfest time scale emerges out of the quantum mechanical coarse-graining of phase-space and the partial resolution of scattering bands. It is the time it takes for quantum mechanical uncertainties to blow up to some relevant classical scale \mathcal{L} in chaotic systems. The scale \mathcal{L} depends on the problem at hand, e.g. on whether the system is closed [16], or open [28, 30]. For the transport set-up we will focus on, this scale is related to the area of scattering bands. Large scattering bands, those with phase-space area greater than $2\pi\hbar$, can carry a number of modes of order their phase-space area divided by $2\pi\hbar$. All those modes are classical, deterministic and exhibit no quantum effects. They are supported by trajectories shorter than the Ehrenfest time. The small bands on the other hand, those with area less than $2\pi\hbar$ carry less than a full mode, which generates quantum (stochastic) modes, sitting on many small bands with dwell times longer than the Ehrenfest time, and hence being partially transmitted and partially reflected. Eq. (6) then defines two open cavity Ehrenfest times for states injected from the L lead, one for transmitting bands and one for reflecting bands

$$\tau_E^{LK} = \lambda^{-1} \ln \left[\frac{W_L W_K}{2\pi\hbar_{\text{eff}} L^2} \right] \quad ; \quad K = \text{L, R}. \quad (8)$$

The difference between τ_E^{LR} and τ_E^{LL} is only logarithmic in W_R/W_L . We will often neglect it and consider instead the symmetric open cavity Ehrenfest time $\tau_E = \lambda^{-1} \ln[(W/L)^2/2\pi\hbar_{\text{eff}}]$. The open cavity Ehrenfest times, τ_E^{LK} can be interpreted as the time it takes for a wavepacket of width W_L/L along the stable manifold of the hyperbolic classical dynamics to evolve into a wavepacket with width W_K/L in the unstable direction.

We can readily estimate the number of quantum scattering modes. The proportion of the L lead phase-space which couples to trajectories to the K lead with $\tau > \tau_E^{LK}$ is on average $e^{-\tau_E^{LK}/\tau_D} W_K/(W_L + W_R)$. Thus the average number of quantum modes in the L lead is

$$\langle N_L^{\text{qm}} \rangle = N_L \frac{N_L e^{-\tau_E^{LL}/\tau_D} + N_R e^{-\tau_E^{LR}/\tau_D}}{N_L + N_R}. \quad (9)$$

All other modes of the L lead are in transmission bands with $\tau < \tau_E^{LR}$ or reflection bands with $\tau < \tau_E^{LL}$, and so they are all classical modes. Their number is thus

$$\begin{aligned} \langle N_L^{\text{cl}} \rangle &= N_L - \langle N_L^{\text{qm}} \rangle \\ &= N_L (1 - e^{-\tau_E^{LR}/\tau_D}) + \mathcal{O}[(\lambda\tau_D)^{-1}]. \end{aligned} \quad (10)$$

The counting argument leading to these estimates finds a rigorous derivation below in section III B, where we explicitly cover scattering bands with an orthonormal phase-space (PS) basis. There, we also identify a third class of states, overlapping significantly but still only partially with large bands with $\tau < \tau_E^{LK}$. Because of their

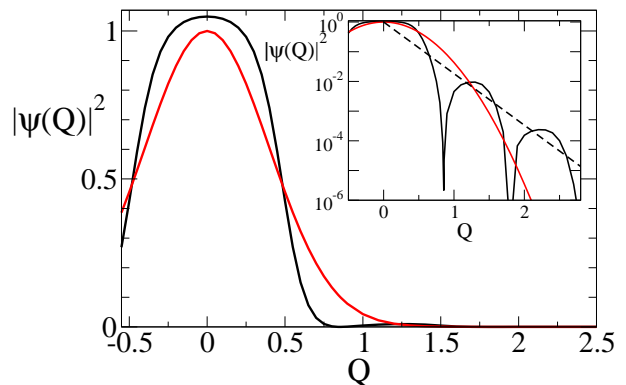


FIG. 6: (Color online) Main plot: Plot of the real-space wavefunction components $|\langle Q|\text{ps}; 0, 0\rangle|^2$ of a PS-basis state (black line), and $|\langle Q|\text{cs}; 0, 0\rangle|^2$ of a coherent state (red line). Both wavefunctions are symmetric in the dimensionless phase-space under $Q \leftrightarrow P$, up to a scaling factor. Inset: Logarithmic plot of $|\langle Q|\text{ps}; 0, 0\rangle|^2$, showing that the PS-state decays exponentially in position (dashed line). The oscillations in $|\langle Q|\text{ps}; 0, 0\rangle|^2$ ensures it is orthogonal to PS-states centered at finite Q , while its broader central peak ensures that it is orthogonal to PS-states centered at finite P .

small relative number however, these states only have a subdominant effect on the system's properties.

Note that the number of classical PS-states goes like $\hbar_{\text{eff}}^{-1}(1 - \hbar_{\text{eff}}^{-1/(\lambda\tau_D)})$, while the number of quantum PS-states goes like $\hbar_{\text{eff}}^{-1-1/(\lambda\tau_D)}$. In the semiclassical limit $\hbar_{\text{eff}} \rightarrow 0$ we see that the number of quantum PS-states goes to infinity, while their fraction goes to zero.

III. THE PHASE-SPACE BASIS

In order to formally split classical from quantum modes, our task now is to construct a complete orthonormal basis resolving maximally the scattering band structure of the classical phase-space. This requires an optimal resolution in both real-space and momentum coordinates. To achieve that, we use results from wavelet analysis.

A. Existence of orthogonal phase-space bases

The existence of complete orthonormal bases with states exponentially localized in time and frequency has been proven in the context of wavelet analysis [31]. We use such a basis as a PS-basis, in which each basis state is exponentially localized in position and momentum. We are unaware of any such basis which has closed form expressions for the basis states. There are however numerous algorithms for generating such bases [31]. In Appendix B we give such an algorithm which iteratively orthogonalizes a complete but non-orthogonal basis of coherent states, generating a set of PS-states of the form

shown in Fig. 6. While we give this explicit example, we emphasize that our theory only requires the existence of such a basis. We use the fact that each basis state is exponentially localized in position and momentum, and that any such complete orthonormal basis remains complete and orthonormal under any rotation, translation or area-preserving stretch in phase-space. Having constructed the PS-basis, the transformation which takes us from lead modes to PS-states is unitary since both bases are orthonormal.

B. The optimal phase-space basis

In a recent letter [22], we constructed an orthonormal PS-basis on a square von Neumann lattice. This basis is simple to explain and work with, however, it underestimates the number of classical modes and in particular leads one to predict that the open cavity Ehrenfest time is half its correct value [32]. To obtain the correct value of τ_E , the von Neumann lattice must be adapted to fit in the classical band structures as best as it can. This is done band by band. For parallelogram bands, the procedure is to rotate and stretch the originally square von Neumann lattice to a parallelogram von Neumann lattice. This is illustrated in Fig. 7. Each lattice cell still covers an area $2\pi\hbar$ and the intraband orthogonality is ensured. The interband basis orthogonality is preserved due to the exponentially small overlap of PS-basis states in different bands (classical bands do not overlap thanks to Liouville's theorem; this effect has been termed *Liouville blocking* in Ref. [22]), except for a minority of states lying directly at the boundary of the band which we will deal with below. This procedure can still be applied as long as the band's curvature is not too large, or for bands which look more trapezoidal than parallelogram-like. All one needs to do then is adapt locally the aspect ratio of the von Neumann lattice, as shown on Fig. 8. Bands with small curvatures dominate at short dwell times. However, some bands with larger dwell times inevitably display a fold. For those bands, the procedure is to bend the von Neumann lattice along the axes defined by the eigenvectors of the stability matrix of the classical dynamics at each point in the band's phase-space, as in Fig. 8. The aspect ratio of the lattice is chosen so it obeys Eq. (11) locally. For intermediate values of \hbar_{eff} , the local curvature of the resulting lattice destroys the orthogonality of the PS-states, however, as \hbar_{eff} is reduced further and further, the curvature drops out of the problem, any smooth curve being locally well approximated by a straight line. To formally show that an optimal orthogonal basis can be generated from the square von Neumann basis of Ref. [22] it is thus sufficient to (i) consider parallelogram and trapezoidal bands only, keeping in mind however that (ii) at any finite value of \hbar_{eff} , deviations from parallelogram shape generates additional non-optimal PS-basis states. The latter result from a further orthogonalization (e.g. Gram-Schmidt) required

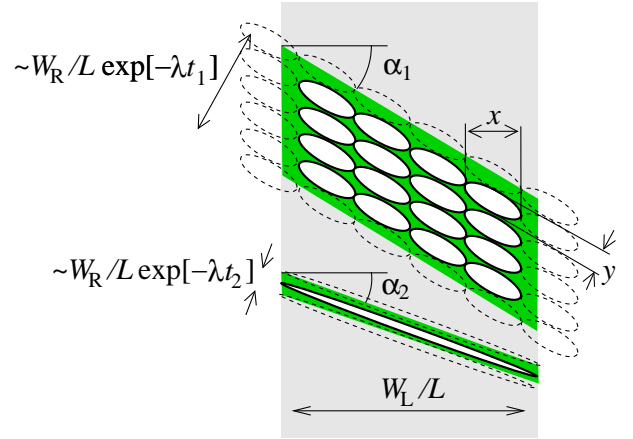


FIG. 7: (Color online) Sketch of two parallelogram bands (green areas) with the PS-states superimposed on them (ellipses). The upper band has a phase-space area which is a bit more than sixteen times $2\pi\hbar$, while the lower band has a phase-space area a bit more than $2\pi\hbar$. In both cases the basis is optimized, the lattice of PS-states is stretched and rotated such that the maximum number of PS-states can be fitted into each band (solid-edged ellipses) with the minimum number partially in the band (dashed-edged ellipses). Note that these optimally chosen PS-states have the same aspect ratio as the classical band in which they sit, thus their longitudinal and transversal extensions, x and y , are given by Eq. (11).

for edge-of-band states and for states on folds whose curvature is not yet well resolved at this value of \hbar_{eff} . Below in Appendix C we will see that those states build up a negligible fraction $N_{\text{qm}}/(\lambda\tau_D) \ll N_{\text{qm}} \ll N_{\text{cl}}$ of the total number of modes in the semiclassical limit. The completeness of the basis follows from the orthogonality and the conservation of the total number of basis states, the above procedure being area-conserving. We are now ready to extend the discussion of Ref. [22] and derive an optimal phase-space basis for parallelogram bands, which gives the correct Ehrenfest time. This is done in a four step process.

Step [i]. Pick a scattering band with phase-space area larger than $2\pi\hbar$, and cover it with a lattice of PS-states. Both the lattice and the states must be stretched and rotated to the same angle and aspect ratio as the band, and positioned in such a way as to minimize the number of edge-of-band states. This is illustrated in Fig. 7. This can be done without relaxing either the mutual orthogonality, or the normalization of the PS-states. Since the PS-states have the same aspect ratio as the band, their longitudinal and transversal extensions x and y , as indicated in Fig. 7, are given by (τ is the dwell time of the band under consideration)[33]

$$x \simeq (2\pi\hbar_{\text{eff}}W_L/W_R)^{1/2} \exp[\lambda\tau/2] ; \quad y \simeq 2\pi\hbar_{\text{eff}}/x. \quad (11)$$

While we pay attention to minimizing their number, we do not include edge-of-band states in the basis at this stage. We will deal with them later in step [iv].

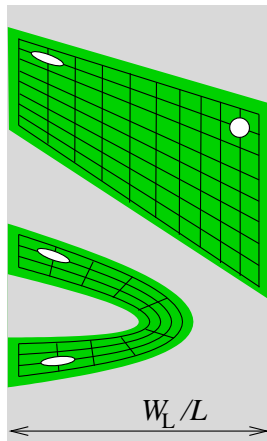


FIG. 8: (Color online) Sketch of a trapezoidal (top green area) and a folded (bottom green area) scattering band with a lattice of PS-states superimposed on them. Both bands cover a phase-space area larger than $2\pi\hbar$. In both cases the basis is optimized, the lattice of PS-states is locally stretched and rotated such that the maximum number of PS-states can be fitted into each band, some of them are indicated by solid-edged ellipses.

Step [ii]. We evolve the states generated in step [i] under the cavity's dynamics. The lattice of PS-states on an injection band uniquely determines the lattice of PS-states on the exit band. All trajectories in the band under consideration exit the cavity after a time shorter than the open cavity Ehrenfest time. On this time scale the quantum dynamics of the PS-states are well approximated by the Liouville flow [34] (see also Appendix A). This is a well-known property of coherent states that can be extended to the exponentially localized PS-states that we consider here. Thus a PS-state with initial spread of ΔQ in the unstable direction at $\tau = 0$, will evolve into a PS-state with spread $\Delta Q' \sim \Delta Q e^{\lambda\tau}$ in the unstable direction at time τ . The initial spread in the stable direction is $\Delta P \simeq \hbar/\Delta Q$, and since the quantum dynamics is Liouvillian inside classical bands, it is area preserving, i.e. $\Delta P' \simeq \hbar/\Delta Q'$. The PS-states are stretched and rotated in the same manner as the exiting band, while still forming an orthonormal basis on that band. The orientation and stretch of the lattice and PS-states are given in linear approximation (which eventually become valid as $\hbar_{\text{eff}} \rightarrow 0$) by the eigenvalues and eigenvectors of the stability matrix of the classical dynamics, and thus have the same aspect ratio and angle as the exiting band. We choose to use these states to cover that band in the phase-space.

Step [iii]. We simply repeat the process in steps [i-ii] for each band with area $> 2\pi\hbar$ not yet covered by PS-states. The crucial point here is that bands cannot overlap; hence if we only place PS-states within classical bands, Liouville blocking ensures that PS-states in different bands must be orthogonal with exponential accuracy.

Step [iv]. Steps [i-iii] generate an incomplete orthonormal basis in the vector-space of lead modes. This basis can be made complete by adding the adequate number of states orthogonal to those generated in steps [i-iii]. This construction gives us very little information about the nature of these additional states, except that they must sit on more than one band. They thus evolve in a quantum, stochastic manner, and we refer to them as quantum PS-states. The set of quantum PS-states divides into two broad categories: firstly those which sit on many classical bands, secondly those which sit mostly, but not completely on a single band. We already mentioned the second category of edge-of-band PS-states (the dashed ellipses in Fig. 7). In Appendix C we estimate that the number of edge-of-band PS-state is

$$N_{\text{eob}} \simeq (\lambda\tau_D)^{-1} N_{\text{qm}} \quad (12)$$

Hence they form a small fraction of the total number of quantum modes, and we do not consider them separately from pure quantum modes.

IV. SCATTERING MATRIX IN THE PHASE-SPACE BASIS

A. Splitting of the scattering matrix and deterministic transmission

By construction, the PS-basis is chosen so that there is a one-to-one correspondence between incoming and outgoing classical PS-states, given that their quantum dynamics can be approximated by the Liouvillian flow. The unitarity of the scattering matrix means that the quantum PS-states remain orthogonal to the classical ones as they evolve inside the cavity. Thus, despite the fact that quantum PS-states are not well described by the Liouvillian flow, they cannot penetrate the regions of phase-space containing bands larger than $2\pi\hbar_{\text{eff}}$. In the PS-basis, each incoming classical PS-state goes to exactly one outgoing classical PS-state, while each incoming quantum PS-state goes to multiple outgoing quantum PS-states, but no outgoing classical PS-states. Correspondingly, the scattering matrix in the PS-basis is of the form

$$\mathcal{S} = \mathcal{S}_{\text{cl}} \oplus \mathcal{S}_{\text{qm}} = \begin{pmatrix} \mathcal{S}_{\text{cl}} & 0 \\ 0 & \mathcal{S}_{\text{qm}} \end{pmatrix}. \quad (13)$$

The matrix \mathcal{S}_{cl} is $N^{\text{cl}} \times N^{\text{cl}}$ while the matrix \mathcal{S}_{qm} is $N^{\text{qm}} \times N^{\text{qm}}$, with $N^{\text{cl}} = N_L^{\text{cl}} + N_R^{\text{cl}}$ and $N^{\text{qm}} = N_L^{\text{qm}} + N_R^{\text{qm}}$.

The matrix \mathcal{S}_{cl} has only one non-zero element in each row and each column. The modes on the left and right of \mathcal{S} can be reordered such that the transmission part \mathbf{t}_{cl} of \mathcal{S}_{cl} is diagonal with all its non-zero elements in the first n elements of its diagonal, where n is the number of classical transmission modes. Thus we can write

$$\mathbf{t}_{\text{cl}} = \begin{pmatrix} \tilde{\mathbf{t}}_{\text{cl}} & 0 \\ 0 & 0 \end{pmatrix}, \quad (14)$$

where all non zero-elements of \mathbf{t}_{cl} are contained in the $n \times n$ matrix $\tilde{\mathbf{t}}_{\text{cl}}$. Doing the same for \mathbf{t}'_{cl} , \mathbf{r}_{cl} and \mathbf{r}'_{cl} , we write the classical part of the scattering matrix as

$$\mathcal{S}_{\text{cl}} \equiv \begin{pmatrix} \mathbf{r}_{\text{cl}} & \mathbf{t}'_{\text{cl}} \\ \mathbf{t}_{\text{cl}} & \mathbf{r}'_{\text{cl}} \end{pmatrix} = \begin{pmatrix} 0 & 0 & \tilde{\mathbf{t}}'_{\text{cl}} & 0 \\ 0 & \tilde{\mathbf{r}}_{\text{cl}} & 0 & 0 \\ \tilde{\mathbf{t}}_{\text{cl}} & 0 & 0 & 0 \\ 0 & 0 & 0 & \tilde{\mathbf{r}}'_{\text{cl}} \end{pmatrix}, \quad (15)$$

where $\tilde{\mathbf{t}}_{\text{cl}}$ and $\tilde{\mathbf{t}}'_{\text{cl}}$ are $n \times n$ matrices, $\tilde{\mathbf{r}}_{\text{cl}}$ is an $(N_L^{\text{cl}} - n) \times (N_L^{\text{cl}} - n)$ matrix and $\tilde{\mathbf{r}}'_{\text{cl}}$ is an $(N_R^{\text{cl}} - n) \times (N_R^{\text{cl}} - n)$ matrix. The matrix $\tilde{\mathbf{t}}_{\text{cl}}$ is diagonal with elements given by

$$(\tilde{\mathbf{t}}_{\text{cl}})_{ij} = e^{i\Phi_i} \delta_{ij}. \quad (16)$$

The matrix $\tilde{\mathbf{r}}_{\text{cl}}$ also has exactly one non-zero element in each row and each column. Its elements obey

$$|(\tilde{\mathbf{r}}_{\text{cl}})_{ij}| = |(\tilde{\mathbf{r}}_{\text{cl}})_{ji}| = \begin{cases} 1 & \text{when } i \text{ reflects to } j, \\ 0 & \text{otherwise.} \end{cases} \quad (17)$$

Anticipating discussions to come, we note that coherent backscattering is carried here by matrix elements $(\tilde{\mathbf{r}}_{\text{cl}})_{ij}$ where the j denotes the time-reversal of i . Since the classical probability to go from i to its time-reversal is equal to the probability to go from i to itself, the number of nonzero such matrix elements is determined by the probability to sit on a periodic orbit which does not visit the contact to any of the two leads except for one point. This probability is zero. The absence of reflection matrix elements carrying coherent backscattering in $\tilde{\mathbf{r}}_{\text{cl}}$ qualitatively explains the exponential suppression of coherent backscattering.

We next calculate the transmission matrix, $\mathbf{T} = \mathbf{t}^\dagger \mathbf{t}$. The block diagonal nature of \mathcal{S} in the PS-basis given in Eq. (13), ensures that \mathbf{T} has the same structure in that basis, hence

$$\mathbf{T} = \mathbf{T}_{\text{cl}} \oplus \mathbf{T}_{\text{qm}} = \begin{pmatrix} \mathbf{T}_{\text{cl}} & 0 \\ 0 & \mathbf{T}_{\text{qm}} \end{pmatrix}, \quad (18a)$$

$$\mathbf{T}_{\text{cl}} = \mathbf{t}_{\text{cl}}^\dagger \mathbf{t}_{\text{cl}} \quad ; \quad \mathbf{T}_{\text{qm}} = \mathbf{t}_{\text{qm}}^\dagger \mathbf{t}_{\text{qm}}. \quad (18b)$$

From Eq. (14,16) we get the eigenvalues of \mathbf{T}_{cl} ,

$$T_i = \begin{cases} 1 & \text{for } 1 \leq i \leq n, \\ 0 & \text{for } n < i \leq N_L^{\text{cl}}. \end{cases} \quad (19)$$

This is what we believe is the first proof of a longstanding hypothesis, that in the classical limit the vast majority of transmission eigenvalues are zero or one [19]. We know that there are N_L^{cl} such classical modes, with the remaining modes having a quantum nature, making them unlikely to have transmission eigenvalues which are exactly zero or one. The block-diagonal structure (18) of the transmission matrix means that the dimensionless conductance, $g = \sum_i T_i$ and the Fano factor for shot noise of Eq. (2), can be written as

$$g = g_{\text{cl}} + g_{\text{qm}}, \quad (20)$$

$$F = \frac{g_{\text{cl}} F_{\text{cl}} + g_{\text{qm}} F_{\text{qm}}}{g_{\text{cl}} + g_{\text{qm}}}. \quad (21)$$

where we have introduced the conductance and Fano factor for the two cavities (classic and quantum), $g_{\text{cl,qm}} = \sum_{i \in \text{cl,qm}} T_i$ and $F_{\text{cl,qm}} = [\sum_{i \in \text{cl,qm}} T_i (1 - T_i)] / [\sum_{i \in \text{cl,qm}} T_i]$. From Eq. (19) we see that

$$g_{\text{cl}} = n \quad ; \quad F_{\text{cl}} = 0. \quad (22)$$

Anticipating the calculation of the average values $\langle g_{\text{cl,qm}} \rangle$ (see next subsection),

$$F = F_{\text{qm}} \exp[-\tau_E^{\text{LR}} / \tau_D]. \quad (23)$$

Since $F_{\text{qm}} < 1$, one see there is an exponential suppression of F .

The PS-basis does not give us much information about the quantum PS-states. However since each incoming PS-state sits on multiple bands, exiting at different times, it must couple to multiple outgoing PS-states. It is extremely rare for these outgoing PS-states to be all transmitting (or all reflecting), and thus we expect that the vast majority of their transmission eigenvalues lie between zero and one, and thus contribute to shot-noise. However the fact that quantum and classical PS-states exist in two separate sub-blocks of the scattering and transmission matrices, see Eqs. (13) and (18), establishes the two-phase fluid model [7].

B. The average Drude conductance

From the estimates in Section II B, the ensemble-averaged Drude conductance is the sum of the Drude conductances of the quantum and classical cavities,

$$\langle g \rangle_D = \langle g_{\text{qm}} \rangle + \langle g_{\text{cl}} \rangle, \quad (24a)$$

$$\langle g_{\text{qm}} \rangle = \frac{N_L^{\text{qm}} N_R^{\text{qm}}}{N_L^{\text{qm}} + N_R^{\text{qm}}} = \frac{N_L N_R}{N_L + N_R} e^{-\tau_E^{\text{LR}} / \tau_D}, \quad (24b)$$

$$\begin{aligned} \langle g_{\text{cl}} \rangle &= \frac{N_L^{\text{cl}} N_R^{\text{cl}}}{N_L^{\text{cl}} + N_R^{\text{cl}}} \\ &= \frac{N_L N_R}{N_L + N_R} [1 - e^{-\tau_E^{\text{LR}} / \tau_D}]. \end{aligned} \quad (24c)$$

Thus the ensemble averaged Drude conductance is,

$$\langle g \rangle_D = N_L N_R / (N_L + N_R). \quad (25)$$

The splitting of the cavity has little effect on $\langle g \rangle_D$, even though classical modes and quantum modes do not mix. For strong asymmetry there is an additional term of order $N_L (\lambda \tau_D)^{-2}$ on the right of Eq. (24c), however our calculation is not valid to that order because we ignored various order $(\lambda \tau_D)^{-1}$ terms, such as edge-of-band states, in Eq. (10).

C. Sample-to-sample conductance fluctuations

The precise shape, size and number of the nonergodic phase-space structures fluctuates from sample to sample.

These fluctuations strongly affect g_{cl} . They are of a classical nature, and as such they induce the departure of conductance fluctuations from their universal behavior [6, 7]. Indeed, once \hbar_{eff} is small enough that quantum mechanics resolves the largest scattering band on average, the sample-to-sample conductance fluctuations are dominated by the band fluctuations. Since each resolved band carries a number $\propto \hbar_{eff}^{-1}$ of channels, one expects sample-to-sample conductance fluctuations to exceed the universal value in the semiclassical limit,

$$\sigma(g_{cl}) \propto \hbar_{eff}^{-1} \gg 1. \quad (26)$$

The above argument predicts the onset for deviations of $\sigma(g)$ from its universal behavior once the largest band is quantum mechanically resolved, i.e. for $\hbar_{eff} < (W/L)^2 \exp[-\lambda\tau_0]$, where τ_0 is the minimal escape time, of order the time of flight through the cavity. Both this onset and the magnitude (26) of the sample-to-sample conductance fluctuations have been observed numerically [6, 7].

V. WEAK LOCALIZATION

We calculate the leading order quantum correction to the Drude conductance. Our treatment applies both to the universal ($\tau_E/\tau_D \rightarrow 0$) and deep semiclassical (finite τ_E/τ_D) regimes. We present an explicit treatment of the coherent backscattering peak showing that our theory preserves the unitarity of the scattering matrix, as well as a calculation of the magnetoconductance. Thus far we have constructed a special basis (the ps-basis) which is aligned along the band structures in the classical phase-space. This made it easy to calculate the properties of the parts of phase-space covered by bands larger than $2\pi\hbar$, allowing us to calculate the deterministic transmission eigenvalues $T = 0, 1$. However the complexity of the quantum modes of that basis, make it difficult to explicitly calculate the transport properties of those modes [21]. We therefore return to the lead-mode basis to calculate weak localization. Unlike previous works we do not neglect the classical bands, however. Indeed, our semiclassical approach is able to extract the conductance (including weak localization) of both the classical and quantum cavities.

A. Drude conductance

Semiclassically, the transmission matrix reads [11, 35],

$$t_{ji} = -(2\pi i \hbar)^{-1/2} \int_L dy_0 \int_R dy \sum_{\gamma} (dp_y/dy_0)_{\gamma}^{1/2} \times \langle j|y \rangle \langle y_0|i \rangle \exp[iS_{\gamma}/\hbar + i\pi\mu_{\gamma}/2], \quad (27)$$

where $|i\rangle$ is the transverse wavefunction of the i th lead mode. This expression sums over all trajectories γ (with

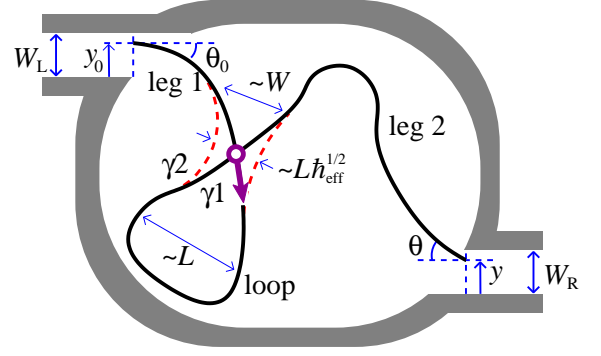


FIG. 9: (Color online) Sketch of the leading order quantum correction to the conductance. Trajectory γ_1 (solid line) is injected at $\mathbf{Y}_0 = (y_0, \theta_0)$, crosses itself and escapes at $\mathbf{Y} = (y, \theta)$. Its first visit to the crossing (the open dot) occurs at $\mathbf{R}_1 = (\mathbf{r}_1, \phi_1)$, where \mathbf{r}_1 is the position in the cavity, and ϕ_1 is the angle of the momentum to a reference axis (not shown). Trajectory γ_2 (dashed line) starts and ends at the same positions as γ_1 , however it avoids the crossing. We divide γ_1 into three segments; leg1, loop and leg2.

classical action S_{γ} and Maslov index μ_{γ}) starting at y_0 on a cross-section of the injection (L) lead and ending at y on the exit (R) lead. Inserting Eq. (27) in the Landauer-Büttiker formula for the conductance $g = \text{Tr}[\mathbf{t}^\dagger \mathbf{t}]$, one gets a double sum over trajectories, γ_1 and γ_2 and over lead modes, $|n\rangle$ and $|m\rangle$. We make the semiclassical approximation that $\sum_n \langle y'|n \rangle \langle n|y \rangle \simeq \delta(y' - y)$ [36]. The conductance is then given by a double sum over trajectories which both go from y_0 on lead L to y on lead R,

$$\text{Tr}[\mathbf{t}^\dagger \mathbf{t}] = \frac{1}{(2\pi\hbar)} \int_L dy_0 \int_R dy \sum_{\gamma_1, \gamma_2} A_{\gamma_1} A_{\gamma_2} e^{i\delta S/\hbar}. \quad (28)$$

Here, $A_{\gamma} = [dp_y/dy_0]_{\gamma}^{1/2}$. Reflection, $R = \text{Tr}[\mathbf{r}^\dagger \mathbf{r}]$, is given by the same expression, with both y_0 and y on lead L. We are interested in quantities averaged over variations in the energy or the cavity shape. For most $\{\gamma_1, \gamma_2\}$ the phase of a given contribution, $\delta S/\hbar$, will oscillate wildly with these variations, so the contribution averages to zero. The most obvious contributions that survive averaging are the diagonal ones with $\gamma_1 = \gamma_2$. These contributions give the Drude conductance (25).

We define $P(\mathbf{Y}, \mathbf{Y}_0; t) \delta y \delta \theta \delta t$ as the product of the initial momentum along the injection lead, $p_F \cos \theta_0$, and the classical probability to go from an initial position and momentum angle $\mathbf{Y}_0 = (y_0, \theta_0)$ to within $(\delta y, \delta \theta)$ of $\mathbf{Y} = (y, \theta)$ in a time within δt of t . Then the sum over all trajectories γ from y_0 to y is

$$\sum_{\gamma} A_{\gamma}^2 [\dots]_{\gamma} = \int_0^\infty dt \int_{-\pi/2}^{\pi/2} d\theta_0 \int_{-\pi/2}^{\pi/2} d\theta \times P(\mathbf{Y}, \mathbf{Y}_0; t) [\dots]_{\mathbf{Y}_0}. \quad (29)$$

For an individual system, P has δ -functions for all classical trajectories. However averaging over an ensemble of

systems or over energy gives a smooth function

$$\langle P(\mathbf{Y}, \mathbf{Y}_0; t) \rangle = \frac{p_F \cos \theta_0 \cos \theta}{2(W_L + W_R)\tau_D} \exp[-t/\tau_D]. \quad (30)$$

This latter expression (30) is valid as long as no restriction is imposed on the trajectory inside the cavity. Using Eqs. (29) and (30) to calculate the conductance within the diagonal approximation, one recovers the Drude conductance (25),

$$g_{\text{diag}} = g_D = \frac{N_L N_R}{N_L + N_R}, \quad (31a)$$

$$R_{\text{diag}} = \frac{N_L^2}{N_L + N_R}. \quad (31b)$$

One also sees that at the level of the diagonal approximation, there is unitarity. We stress that, unlike in Ref. [37], we do not include coherent backscattering in the diagonal contribution, it is dealt with separately below.

B. Weak localization for transmission

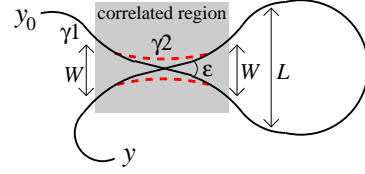
A pair of trajectories giving the leading order correction to the Drude conductance is shown in Fig. 9. The trajectories are paired almost everywhere except in the vicinity of an encounter [37]. Going through an encounter, one of the trajectories intersects itself, while the other one avoids the crossing. Thus, they travel along the loop they form in opposite direction. It has been shown in Ref. [38] that for any self-intersecting trajectory with a small enough crossing angle ϵ , there exists a partner, crossing-avoiding outer trajectory. For the relevant case of small ϵ , the probability to find a weak localization pair is thus given by the probability to find a self-intersecting trajectory. The two trajectories are always close enough to each other that their stability is the same, i.e. one can set $\sum_{\gamma_1, \gamma_2} A_{\gamma_1} A_{\gamma_2} \rightarrow \sum_{\gamma_1} A_{\gamma_1}^2$. To evaluate the weak localization correction to conductance, we perform a calculation similar to Ref. [37], adding the crucial fact that pair of trajectories such as depicted in Fig. 9 have highly correlated escape probabilities due to the presence of an encounter [27]. The situation is depicted in more detail in Fig. 10.

The presence of the encounter introduces two new ingredients, both of these were overlooked in Ref. [37]. First, pairs of trajectories leaving an encounter escape the cavity in either a correlated or an uncorrelated way. Uncorrelated escape occurs when the perpendicular distance between the trajectories is larger than the width $W_{L,R}$ of the leads. This requires a minimal time $T_W(\epsilon)/2$ between encounter and escape, where [39]

$$T_W(\epsilon) = \lambda^{-1} \ln[\epsilon^{-2}(W/L)^2]. \quad (32)$$

The two pairs of trajectories then escape in an uncorrelated manner, typically at completely different times, with completely different momenta (and possibly through

(a) Weak-localization for transmission (conductance)



(b) Weak-localization and coherent back-scattering for reflection

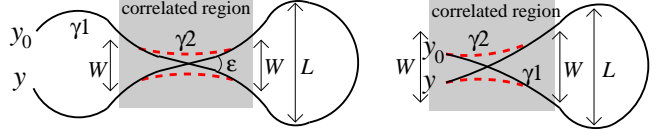


FIG. 10: (Color online) Sketches of the trajectory pairing which give the leading off-diagonal contributions to (a) transmission (conductance) and (b) reflection. All contributions involve a trajectory γ_1 crossing itself at an angle ϵ , and a trajectory γ_2 which avoids the crossing. The action difference between the two trajectories is thus small and does not fluctuate under averaging. For transmission, y_0 is on L lead and y is on R lead, for reflection both y_0 and y are on L lead. There are two reflection contributions. On the left is weak localization, and on the right is coherent backscattering (details of the latter are in Fig. 12).

different leads). Correlated escape occurs in the other situation when the distance between the trajectories at the time of escape is less than $W_{L,R}$. Then the two pairs of trajectories escape together, at the same time through the same lead. This latter process affects coherent backscattering (see Fig. 10). The second new ingredient is that the survival probability for a trajectory with an encounter is larger than that of a generic trajectory. This is so, because the encounter duration affects the escape probability only once. In other words, if the trajectory did not escape in its first passage through the encounter, neither will it during its second passage (this was first noticed in Ref. [27]).

We calculate the contribution from pairs of transmitting trajectories sketched in Fig. 10a. For preserved time-reversal symmetry, the action difference for this contribution is $\delta S_{\text{wl}} = E_F \epsilon^2 / \lambda$ [37]. We now note that the probability to go from \mathbf{Y}_0 to \mathbf{Y} in time t , is the product of the probability to go from \mathbf{Y}_0 to a point on the energy surface inside the cavity $\mathbf{R}_1 = (\mathbf{r}_1, \phi_1)$ (where ϕ_1 defines the direction of the momentum) in time t_1 and the probability to go from \mathbf{R}_1 to \mathbf{Y} in time $t - t_1$, when one integrates \mathbf{R}_1 over the energy surface \mathcal{C} . Thus the quantity P introduced above can be written as

$$P(\mathbf{Y}, \mathbf{Y}_0; t) = \int_{\mathcal{C}} d\mathbf{R}_2 d\mathbf{R}_1 \tilde{P}(\mathbf{Y}, \mathbf{R}_2; t - t_2) \times \tilde{P}(\mathbf{R}_2, \mathbf{R}_1; t_2 - t_1) P(\mathbf{R}_1, \mathbf{Y}_0; t_1). \quad (33)$$

where $\tilde{P}(\mathbf{R}_2, \mathbf{R}_1; t)$ is the probability density to go from \mathbf{R}_1 to \mathbf{R}_2 in time t , but $P(\mathbf{R}_1, \mathbf{Y}_0; t)$ is a probability density multiplied by the injection momentum, $p_F \cos \theta_0$.

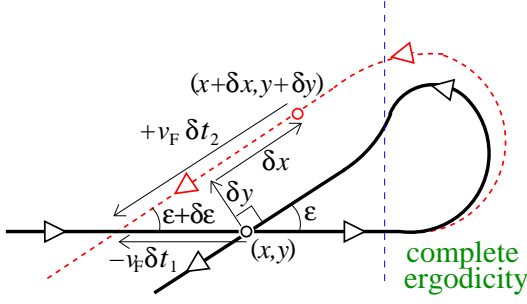


FIG. 11: (Color online) Sketch of a trajectory (solid line) which crosses itself at point $\mathbf{r}_1 = (x, y)$, visiting this point first at time t_1 and second at time t_2 . Superimposed is an infinitesimally different trajectory (dashed line) which also visits the point (x, y) at t_1 , but is at point $\mathbf{r}_2 = (x + \delta x, y + \delta y)$ at time t_2 . This trajectory also intersects itself; however, it visits the self-intersection (which is no longer (x, y)) at times $t_1 + \delta t_1$ and $t_2 + \delta t_2$.

We then restrict the probabilities inside the integral to trajectories which cross themselves at phase-space positions $\mathbf{R}_{1,2}$ with the first (second) visit to the crossing occurring at time t_1 (t_2). Using Fig. 11, we write $d\mathbf{R}_2 = v_F^2 \sin \epsilon dt_1 dt_2 d\epsilon$ and set $\mathbf{R}_2 \equiv (\mathbf{r}_2, \phi_2) = (\mathbf{r}_1, \phi_1 \pm \epsilon)$. Next, we note that the duration of the loop must exceed $T_L(\epsilon) = \lambda^{-1} \ln[\epsilon^{-2}]$, because for shorter times, two trajectories leaving an encounter remain close enough to each other that their relative dynamics is hyperbolic, and the probability of forming a loop is zero. Similarly the path cannot transmit unless $t_1, t - t_2 > T_W(\epsilon)$, because for $t_1, t - t_2 < T_W(\epsilon)$ the legs (see Fig. 9) are so close to each other that if one leg escapes through a given lead the other one will escape with it through the *same* lead. Thus the probability that a trajectory starting at \mathbf{Y}_0 crosses itself at an angle $\pm \epsilon$ and then transmits, multiplied by its injection momentum $p_F \cos \theta_0$, is

$$I(\mathbf{Y}_0, \epsilon) = 2v_F^2 \sin \epsilon \int_{T_L + T_W}^{\infty} dt \int_{T_L + T_W/2}^{t - T_W/2} dt_2 \int_{T_W/2}^{t_2 - T_L} dt_1 \times \int_{\mathbf{R}} d\mathbf{Y} \int_{\mathbf{C}} d\mathbf{R}_1 \tilde{P}(\mathbf{Y}, \mathbf{R}_2; t - t_2) \times \tilde{P}(\mathbf{R}_2, \mathbf{R}_1; t_2 - t_1) P(\mathbf{R}_1, \mathbf{Y}_0; t_1), \quad (34)$$

where T_W, T_L are shorthand for $T_W(\epsilon), T_L(\epsilon)$.

To get the weak localization correction to conductance we sum only contributions where γ_1 crosses itself, we then take twice the real part of this result to include the contributions where γ_1 avoids the crossing (and hence γ_2 crosses itself). Thus

$$g_{wl} = (\pi \hbar)^{-1} \int_{\mathbf{L}} d\mathbf{Y}_0 d\epsilon \text{Re}[e^{i\delta S_{wl}/\hbar}] \langle I(\mathbf{Y}_0, \epsilon) \rangle. \quad (35)$$

We perform the average of the P s as follows. Within $T_W(\epsilon)/2$ of the crossing the two legs of a self-intersecting trajectory are so close to each other that their joint escape probability is the same as for a single trajectory.

Self-intersecting trajectories thus have an enhanced survival probability compared to non-crossing trajectories of the same length, i.e. the duration of the crossing must be counted only once in the survival probability [27]. Outside the correlated region, the legs can escape independently through either lead at anytime. Furthermore, the probability density for the trajectory going to a given point in phase-space is assumed to be uniform. Thus the probability density for leg 1 gives $\langle P(\mathbf{R}_1, \mathbf{Y}_0; t_1) \rangle = (2\pi A)^{-1} \exp(-t_1/\tau_D) \times p_F \cos \theta_0$, and the loop's probability density is $\langle \tilde{P}(\mathbf{R}_2, \mathbf{R}_1; t_2 - t_1) \rangle = (2\pi A)^{-1} \exp\{-[t_2 - t_1 - T_W(\epsilon)/2]/\tau_D\}$ (Ref. [40]). Finally the *conditional* probability density for leg 2 (given that leg 1 exists for a time $t_1 > T_W(\epsilon)$) is $\langle \tilde{P}(\mathbf{Y}, \mathbf{R}_2; t - t_2) \rangle = [2(W_L + W_R)\tau_D]^{-1} \cos \theta \exp\{-[t - t_2 - T_W(\epsilon)/2]/\tau_D\}$. Hence one finds

$$\langle \tilde{P}(\mathbf{Y}, \mathbf{R}_2; t - t_2) \tilde{P}(\mathbf{R}_2, \mathbf{R}_1; t_2 - t_1) P(\mathbf{R}_1, \mathbf{Y}_0; t_1) \rangle = \frac{1}{(2\pi A)^2} \frac{p_F \cos \theta \cos \theta_0}{2(W_L + W_R)\tau_D} \exp[-(t - T_L(\epsilon))/\tau_D], \quad (36)$$

so that $\langle I(\mathbf{Y}_0, \epsilon) \rangle$ becomes

$$\langle I(\mathbf{Y}_0, \epsilon) \rangle = \frac{(v_F \tau_D)^2}{\pi A} p_F \sin \epsilon \cos \theta_0 \times \frac{N_R}{N_L + N_R} \exp[-T_L(\epsilon)/\tau_D]. \quad (37)$$

We insert this into Eq. (35). The ϵ -integral is dominated by contributions with $\epsilon \ll 1$, so that we write $\sin \epsilon \simeq \epsilon$ and push the upper bound for the ϵ -integration to infinity. The ϵ -integral can then be computed to give an Euler Γ -function [25]. To leading order in $(\lambda \tau_D)^{-1}$ it equals $-\pi \hbar (2E_F \tau_D)^{-1}$. The integral over \mathbf{Y}_0 yields a factor of $2W_L$. Finally noting that $N_L = (\pi \hbar)^{-1} p_F W_L$ and $(N_L + N_R)^{-1} = (mA)^{-1} \hbar \tau_D$, the weak localization correction to the conductance reads

$$g_{wl} = -\frac{N_L N_R}{(N_L + N_R)^2} \exp[-\tau_E^{cl}/\tau_D]. \quad (38)$$

We see that weak localization is exponentially suppressed with τ_E^{cl}/τ_D in term of the closed cavity Ehrenfest time $\tau_E^{cl} \equiv \lambda^{-1}[\hbar_{\text{eff}}^{-1}]$.

C. Quantum corrections to reflection

The above result (38) has already been derived in Ref. [25] by a similar approach. We go beyond that by showing explicitly that our semiclassics preserves the unitarity of the scattering matrix. There are two leading-order off-diagonal corrections to reflection. They are shown in Fig. 10(b). The first is weak localization while the second is coherent backscattering. The former reduces the probability of reflection to arbitrary momentum, while the latter enhances the probability of reflection to the time-reverse of the injection state. The distinction between these two contributions is whether or

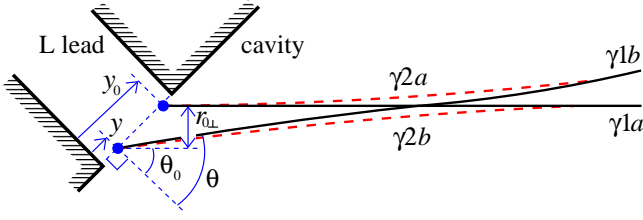


FIG. 12: (Color online) Trajectories for the backscattering contributions to reflection. Trajectory γ_1 (solid black line) start on the cross-section of the L lead at position y_0 with momentum angle θ_0 and ends at y with momentum angle θ . In the basis parallel and perpendicular to γ_1 at injection, the initial position and momentum of path γ_1 at exit are $r_{0\perp} = (y_0 - y) \cos \theta_0$, $r_{0\parallel} = (y_0 - y) \sin \theta_0$ and $p_{0\perp} \simeq -p_F(\theta - \theta_0)$.

not the legs escape while correlated: for weak localization the legs escape independently, while for coherent backscattering the legs escape together in a correlated manner.

1. Weak localization

The weak localization contribution to reflection, R_{wl} , is derived in the same manner as g_{wl} , replacing however a factor of $W_R/(W_L + W_R)$ with $W_L/(W_L + W_R)$. One obtains

$$R_{wl} = -\frac{N_L^2}{(N_L + N_R)^2} \exp[-\tau_E^{cl}/\tau_D] \quad (39)$$

2. Coherent backscattering

Contributions to coherent backscattering are shown in Fig. 10b, with Fig. 12 showing the trajectories in the correlated region in more detail. These contributions require special care because (i) their action phase difference δS_{cbs} is not given by the Richter-Sieber expression used so far and (ii) injection and exit positions and momenta are correlated.

From Fig. 12, and noting that γ_{2b} decays exponentially towards γ_{1a} , we find the action difference between these two path segments to be

$$S_{2b} - S_{1a} = p_F(y_0 - y) \sin \theta_0 + \frac{1}{2} m \lambda (y_0 - y)^2 \cos^2 \theta_0. \quad (40)$$

We have dropped cubic terms which only give \hbar -corrections to the stationary-phase integral. The action difference between γ_{2a} and γ_{1b} has the opposite sign for $y_0 - y$ and θ_0 replaced by θ . We get for the total action difference, in terms of $(r_{0\perp}, p_{0\perp})$,

$$\delta S_{cbs} = -(p_{0\perp} + m \lambda r_{0\perp}) r_{0\perp}. \quad (41)$$

The coherent backscattering contribution to the reflection reads

$$R_{cbs} = (2\pi\hbar)^{-1} \int d\mathbf{Y}_0 d\mathbf{Y} \int_0^\infty dt \times \langle P(\mathbf{Y}, \mathbf{Y}_0; t) \rangle \text{Re}[e^{i\delta S_{cbs}/\hbar}]. \quad (42)$$

Note that this contains all those contributions where γ_1 crosses itself and all those contributions where it avoids crossing (so γ_2 crosses itself), thus there is no need to take twice the real part here (unlike for g_{wl}). To perform the average we define $T'_W(r_{0\perp}, p_{0\perp})$ and $T'_L(r_{0\perp}, p_{0\perp})$ as the times for which the perpendicular distance between the γ_{1a} and γ_{1b} is W and L , respectively. For times less than $T'_W(r_{0\perp}, p_{0\perp})$ the escape probability for two trajectories is the same as for one, while for times longer than this the trajectories evolve and escape independently. For R_{cbs} we consider only those trajectories that form a closed loop, however they cannot close until the two trajectory segments are of order L apart. The t -integrals must have a lower cut-off at $2T'_L(r_{0\perp}, p_{0\perp})$, hence

$$\int_R d\mathbf{Y} \int_{2T'_L}^\infty dt \langle P(\mathbf{Y}, \mathbf{Y}_0; t) \rangle = p_F \cos \theta_0 \frac{N_L}{N_L + N_R} \exp[-T'(r_{0\perp}, p_{0\perp})/\tau_D], \quad (43)$$

where $T'(r_{0\perp}, p_{0\perp}) = 2T'_L(r_{0\perp}, p_{0\perp}) - T'_W(r_{0\perp}, p_{0\perp})$. For small $(p_{0\perp} + m \lambda r_{0\perp})$ we estimate

$$T'(r_{0\perp}, p_{0\perp}) \simeq \lambda^{-1} \ln \left[\frac{W(p_{0\perp} + m \lambda r_{0\perp})}{m \lambda L^2} \right]. \quad (44)$$

We substitute the above expression into R_{cbs} , write $p_F \cos \theta_0 d\mathbf{Y}_0 = dy_0 d(p_F \sin \theta_0) = dr_{0\perp} dp_{0\perp}$ [11], and then make the substitution $\tilde{p}_0 = p_{0\perp} + m \lambda r_{0\perp}$. We evaluate the $r_{0\perp}$ -integral over a range of order W_L , take the limits on the resulting \tilde{p}_0 -integral to infinity and write it in terms of Euler Γ -functions. Finally we systematically drop all terms $\mathcal{O}(1)$ inside logarithms. The result is that

$$R_{cbs} = \frac{N_L}{N_L + N_R} \exp[-\tau_E^{cl}/\tau_D]. \quad (45)$$

Thus we see that coherent backscattering is also suppressed exponentially in exactly the same manner as weak localization. Hence $R_{cbs} + R_{wl} = -g_{wl}$ and unitarity is preserved.

D. The off-diagonal nature of coherent backscattering

Continuous families of trajectories that are present in open chaotic systems, such as γ_2 and γ_1 in Fig. 12, have an action difference given in Eq. (41). This action difference does not fluctuate under energy or sample averaging, moreover, these contributions are not diagonal in the lead mode basis. The stationary phase integral

over such trajectories is dominated by $p_{0\perp} \simeq -m\lambda r_{0\perp}$ where $r_{0\perp}$ is integrated over the total lead width. Thus $p_{0\perp}$ varies over a range of order $m\lambda W \gg \pi\hbar/W$, coupling to many lead modes. Such contributions were not taken into account in the previous analysis of coherent backscattering [37]. This caused the erroneous belief (of the authors of the present article amongst others) that coherent backscattering originates from trajectories that return to any point in the L lead with $\theta \simeq \pm\theta_0$, which would have implied that the coherent backscattering was independent of the Ehrenfest time.

Once we correctly sum the many off-diagonal contributions to $\sum_{nm} |r_{nm}|^2$ which have an encounter near the L lead, we conclude that coherent backscattering approximately doubles the weight of all returning trajectories in a strip defined by

$$\theta - \theta_0 \simeq -p_F^{-1} m\lambda(y - y_0) \cos \theta_0 \quad (46)$$

across the lead. This strip sits on the stable axis of the classical dynamics, with a width in the unstable direction of order $\hbar(p_F W)^{-1}$. Therefore, trajectories in the strip first converge toward each other, and only start diverging at a time of order $\tau_E^{\text{op}}/2$. Such trajectories cannot form a loop on times shorter than $\tau_E^{\text{op}} + \tau_E^{\text{cl}}$.

E. Magnetoconductance

A weak magnetic field has very little effect on the classical dynamics. Its dominant effect is to generate a phase difference between two trajectories that go the opposite way around a closed loop. This phase difference is $\mathcal{A}_{\text{loop}}\Phi$ where $\mathcal{A}_{\text{loop}}$ is the directed area enclosed by the loop, and Φ is the flux in units of the flux quantum. To incorporate this in the theory we must introduce a factor of $\exp[i\mathcal{A}_{\text{loop}}\Phi]$ into $I(\mathbf{Y}_0, \epsilon)$ in Eq. (34) and inside the average in R_{cbs} in Eq. (42). To average $\langle \exp[i\mathcal{A}_{\text{loop}}\Phi] \rangle$, we divide the loop into two parts — the correlated part (within $T_L(\epsilon)/2$ of the crossing), and the uncorrelated part (the rest of the loop). We average the two parts separately.

For the uncorrelated part, we use the fact that the distribution of area enclosed by classical scattering trajectories in a chaotic system is Gaussian with zero mean and a variance which increases linearly with time [11]. One then has,

$$\langle e^{i\mathcal{A}_{\text{uncorr}}\Phi} \rangle = \exp[-\alpha A^2 \Phi^2 (t_2 - t_1 - T_L(\epsilon))/\tau_f], \quad (47)$$

where, A is the area of the cavity, α is a system-dependent parameter of order unity, and τ_f is the time of flight between two consecutive bounces at the cavity's wall.

We comment on the correlated part in Appendix D, where we show that it provides at most only small corrections $\mathcal{O}(\tau_f/\tau_D)$ which we henceforth ignore. Multiplying the integrand in Eq. (34) with (47), and integrating over

t_1, t_2 gives

$$\begin{aligned} \langle I(\mathbf{Y}_0, \epsilon) \rangle &= \frac{(v_F \tau_D)^2}{\pi A} p_F \sin \epsilon \cos \theta_0 \\ &\times \frac{N_R}{N_L + N_R} \frac{\exp[-T_L(\epsilon)/\tau_D]}{1 + \alpha A^2 (\tau_D/\tau_f) \Phi^2}. \end{aligned} \quad (48)$$

After a similar analysis for R_{cbs} , we conclude that for finite flux, the quantum corrections to the average conductance acquire a Lorentzian shape,

$$g_{\text{wl}}(\Phi) = -\frac{N_L N_R}{(N_L + N_R)^2} \frac{\exp[-\tau_E^{\text{cl}}/\tau_D]}{1 + \alpha A^2 (\tau_D/\tau_f) \Phi^2}, \quad (49a)$$

$$R_{\text{wl}}(\Phi) = -\frac{N_L^2}{(N_L + N_R)^2} \frac{\exp[-\tau_E^{\text{cl}}/\tau_D]}{1 + \alpha A^2 (\tau_D/\tau_f) \Phi^2}, \quad (49b)$$

$$R_{\text{cbs}}(\Phi) = \frac{N_L}{N_L + N_R} \frac{\exp[-\tau_E^{\text{cl}}/\tau_D]}{1 + \alpha A^2 (\tau_D/\tau_f) \Phi^2}. \quad (49c)$$

Interestingly enough, there is no Ehrenfest dependence in the width of the Lorentzian.

F. Weak localization in the two-fluid model

Weak localization can also be calculated in the framework of the special basis constructed in the first half of this paper. We can split all contributions to conductance into classical and quantum contributions using the classical dynamics. By construction the classical modes couple to the trajectories shorter than τ_E^{op} , while the quantum ones couple to the ones longer than τ_E^{op} . We cut the time-integrals in all the above quantities at τ_E^{op} , the result is that the classical cavity has

$$g_D^{\text{cl}} = \frac{N_L N_R}{N_L + N_R} [1 - e^{-\tau_E^{\text{op}}/\tau_D}], \quad (50a)$$

$$R_{\text{diag}}^{\text{cl}} = \frac{N_L^2}{N_L + N_R} [1 - e^{-\tau_E^{\text{op}}/\tau_D}], \quad (50b)$$

$$g_{\text{wl}}^{\text{cl}} = R_{\text{wl}}^{\text{cl}} = R_{\text{cbs}} = 0. \quad (50c)$$

The quantum modes carrying the remaining contributions. Inserting by hand the phase-space splitting into the sum rules and bound of time integrations in the above semiclassical treatment, one recovers the exponential suppression of weak localization, Eq. (38). The quantum fluid is thus clearly not RMT, which invalidates the effective RMT model [4]. This is because contributions to weak localization and coherent backscattering come from trajectories longer than $\tau_E^{\text{op}} + \tau_E^{\text{cl}}$, and the proportion of such trajectories in the quantum cavity goes like $\exp[-\tau_E^{\text{cl}}/\tau_D]$.

The existence of classical bands is key to both the existence of the two separate fluids (block diagonal nature of \mathcal{S} , Eq. (13)) and to the exponential suppression of coherent backscattering and the unitarity of the semiclassical theory presented here (see also [21]).

VI. NUMERICAL SIMULATIONS

We finally check our semiclassical theory for weak localization at finite $\tau_E^{\text{cl}}/\tau_D$ against numerical simulations. We consider open systems with fully developed chaotic dynamics, for which $\tau_D \gg 1$. Because τ_E^{cl} grows logarithmically with the Hilbert space size $M = \hbar_{\text{eff}}^{-1}$, and since we want to investigate the regime of finite $\tau_E^{\text{cl}}/\tau_D$, we model the electron dynamics by the kicked rotator map [5, 7, 23]. The Hamiltonian is given by

$$H = \frac{(p + p_0)^2}{2} + K \cos(x + x_0) \sum_n \delta(t - n\tau_f). \quad (51)$$

The kicking strength K drives the dynamics from integrable ($K = 0$) to fully chaotic [$K \gtrsim 7$, with Lyapunov exponent $\lambda\tau_f \approx \ln(K/2)$]. The parameters p_0 and x_0 are introduced to break the Hamiltonian's two symmetries [41]. Only when these two symmetries are broken does one witness a crossover from the $\beta = 1$ to the $\beta = 2$ universality class [13], corresponding to breaking the time reversal symmetry [41]. The procedure of varying p_0 followed in Refs. [26, 27] results in a strongly non-Lorentzian magnetoconductance. Thus the agreement between numerics and analytics in Ref. [27] could not be extended to the magnetoconductance curve, which is the trademark of weak localization. This motivated us to perform numerical investigations following the same procedure as in Ref. [42], i.e. taking a finite, constant p_0 , while varying x_0 . In this case, the magnetoconductance curves are Lorentzian.

We consider a toroidal classical phase-space $x, p \in [0, 2\pi]$, and open the system by defining contacts to ballistic leads via two absorbing phase-space strips $[x_L - \delta x, x_L + \delta x]$ and $[x_R - \delta x, x_R + \delta x]$, each of them with a width $2\delta x = \pi/\tau_D$. We quantize the map by discretizing the momentum coordinates as $p_l = 2\pi l/M$, $l = 1, \dots, M$. A quantum representation of the Hamiltonian (51) is provided by the unitary $M \times M$ Floquet operator U , which gives the time evolution for one iteration of the map. For our specific choice of the kicked rotator, the Floquet operator has matrix elements

$$U_{l,l'} = M e^{-(\pi i/M)[(l+l_0)^2 + (l'+l_0)^2]} \times \sum_m e^{2\pi i m(l-l')/M} e^{-(iMK/2\pi) \cos(2\pi(m+m_0)/M)} \quad (52)$$

with $l_0 = p_0 M/2\pi$ and $m_0 = x_0 M/2\pi$.

We restrict ourselves to the symmetric situation with $N_{R,L} = N$. A $2N \times 2N$ scattering matrix can be constructed from the Floquet operator U as [43]

$$S(\varepsilon) = P[\exp(-i\varepsilon) - U(1 - P^T P)]^{-1} U P^T, \quad (53)$$

using a $2N \times M$ projection matrix P which describes the coupling to the leads. Its matrix elements are given by

$$P_{n,m} = \begin{cases} 1 & \text{if } n = m \in \{m_i^{(R)}\} \cup \{m_i^{(L)}\}, \\ 0 & \text{otherwise.} \end{cases} \quad (54)$$

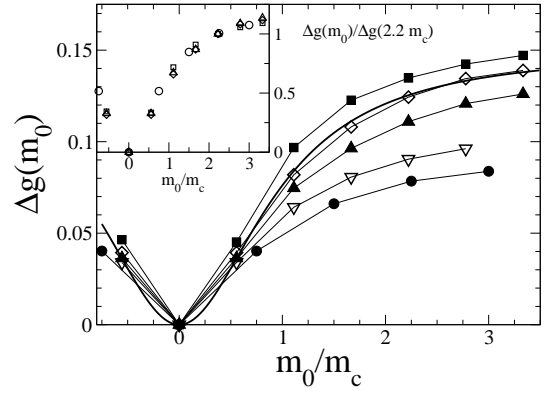


FIG. 13: Magnetoconductance curves $\Delta g(m_0) = g(m_0) - g(0)$ for the open kicked rotator model (defined in the text) at fixed classical configuration $K = 14$ ($\lambda \approx 1.95$), $\tau_D/\tau_f = 5$, and different Hilbert space sizes, $M = 256$ (squares, $\tau_E^{\text{cl}}/\tau_D \approx 0.57$), $M = 512$ (diamonds, $\tau_E^{\text{cl}}/\tau_D \approx 0.64$), $M = 1024$ (upward triangles, $\tau_E^{\text{cl}}/\tau_D \approx 0.71$), $M = 2048$ (downward triangles, $\tau_E^{\text{cl}}/\tau_D \approx 0.78$), and $M = 4096$ (circles, $\tau_E^{\text{cl}}/\tau_D \approx 0.85$). The solid line gives the best Lorentzian fit for the $M = 512$ curve, $\Delta g(m_0) = 0.15 - 0.15/[1 + 1.03 (m_0/m_c)^2]$. Data have been obtained after averaging over 100000 (1000 classically different samples, each with 100 different quasienergies for $M = 256$) to 25000 (500 classically different samples, each with 50 different quasienergies for $M = 4096$) different samples. Inset: rescaled magnetoconductance data, $\Delta g(m_0)/\Delta g(2.2m_c)$, the data collapses onto a single curve, confirming out theory that m_c does not depend on τ_E^{cl} .

An ensemble of samples with the same microscopic parameters can be defined by varying the position $\{m_i^{(R,L)}\}$, $i = 1, \dots, N$ of the contacts to the left and right leads for fixed $\tau_D/\tau_f = M/2N$ and K [τ_f is the time of flight through the system, in this particular instance it is the time between kicks, see (51)]. We calculate the conductance from the scattering matrix, which we numerically construct via an iterative procedure as in Refs. [7, 26].

In the universal regime $\tau_E^{\text{cl}}/\tau_D = 0$, Ref. [42] found, for the $\beta = 1$ to $\beta = 2$ crossover a magnetoresistance given by

$$\delta g = \frac{1}{4} \frac{1}{1 + (m_0/m_c)^2} ; \quad m_c = \frac{4\pi}{\sqrt{M\tau_D K}}, \quad (55)$$

which has to be compared to Eq. (49a). Our task here is to investigate the fate of (55) as $\tau_E^{\text{cl}}/\tau_D$ increases, and in particular to check our analytical predictions (49a) that (i) the magnetoconductance is Lorentzian with (ii) a width which is independent of τ_E^{cl} , but (iii) an amplitude which is suppressed exponentially $\propto \exp[-\tau_E^{\text{cl}}/\tau_D]$.

Fig. 13 shows magnetoconductance curves as $\tau_E^{\text{cl}}/\tau_D$ increases while keeping all classical parameters unchanged. The data confirm our prediction (49a), i.e. the curves are Lorentzian which depend on $\tau_E^{\text{cl}}/\tau_D$ only through their amplitude. The inset of Fig. 13 makes it clear that the typical field necessary to break time-reversal symmetry does not depend on τ_E^{cl} — after rescaling the magnetocon-

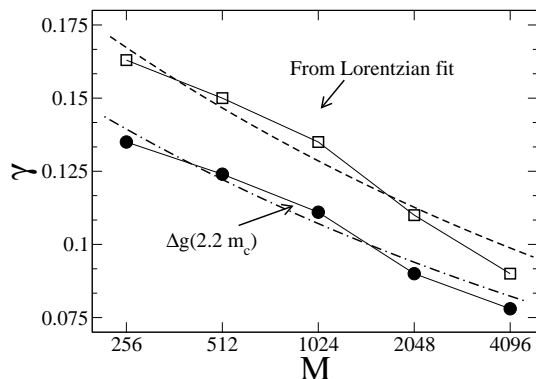


FIG. 14: Amplitude of the weak localization correction to the conductance as a function of the size of Hilbert space. Data have been extracted from the curves shown on Fig. 13 either via a fitting of the magnetoconductance curve with the Lorentzian $\Delta g(m_0) = \gamma - \gamma/[1 + \gamma'(m_0/m_c)^2]$ (squares) or taking $\gamma = \Delta g(2.2m_c)$ (circles). Both methods confirm the exponential suppression $\gamma \propto \exp[-\tau_E^{\text{cl}}/\tau_D]$ (dashed and dotted-dashed lines) with an effectively smaller Lyapunov exponent $\lambda \approx 1.26$ (compared to $\ln[K/2] \approx 1.95$) [44].

ductance amplitude, all curves fall on top of each other. This was also confirmed by least square Lorentzian fitting of the magnetoconductance curves with $\Delta g(m_0) = \gamma - \gamma/[1 + \gamma'(m_0/m_c)^2]$, which found $\gamma' = 1 \pm 0.06$ for all cases.

Fig. 14 finally gives a closer look at the suppression of the amplitude of the weak localization correction. We extracted the amplitude parameter γ both from a least square Lorentzian fitting of the magnetoconductance curve, and from the magnetoconductance amplitude at $m_0 = 2.2m_c$, $g(2.2m_c) - g(0)$. The two procedures confirm the exponential suppression of weak localization (38), in agreement with Ref. [27].

VII. CONCLUSIONS

In this paper we investigated the non-coherent transport properties of open quantum chaotic systems in the semiclassical limit. We have shown how to incorporate the nonergodic structures appearing in the classical phase-space (see Fig. 1) into quantum transport. We followed the scattering approach to transport and showed how large phase-space structures result in a block-diagonal form of the scattering matrix and the splitting of the system into two sub-systems put in parallel. One of these sub-systems is of a purely classical nature, consisting of deterministic transmission modes (transmission eigenvalues are all 0 or 1). We were able to calculate the corresponding transmission eigenvectors and connect the emergence of determinism to the suppression of the Fano factor for shot-noise as well as the breakdown of universality for sample-to-sample conductance fluctuations. The classical phase-space struc-

tures also cause the exponential suppression of coherent backscattering, preserving the unitarity of the semiclassical theory of weak localization presented here.

At this point, the quantum mechanical subsystem is known not to be RMT. Even though all its modes undergo a certain amount of mixing, and thus carry quantum effects, weak localization and coherent backscattering come from trajectories longer than $\tau_E^{\text{op}} + \tau_E^{\text{cl}}$, which have an exponentially small relative weight $\exp[-\tau_E^{\text{cl}}/\tau_D]$ in the quantum cavity. The existence of two separated fluids is however confirmed.

We finally point out that the phase-space method developed in the first half of this article should work as well in regular systems. We however anticipate difficulties not present in the chaotic systems treated here due to the power-law decay of the band areas and diffraction effects at the leads. One open question is why open regular systems with large dwell times have a RMT transmission spectrum [45, 46], but a nonuniversal weak localization behavior [11, 47].

After this work was completed, a preprint appeared which reached the same conclusions about coherent backscattering [48].

Acknowledgments

It is a pleasure to thank İ. Adagideli and H. Schomerus for helpful discussions, and C. Beenakker for drawing our attention to Ref. [42]. This work has been financially supported by the Swiss National Science Foundation.

APPENDIX A: GAUSSIAN WAVEPACKETS AND HYPERBOLIC DYNAMICS

We show that the time-evolution of a Gaussian wavepacket in a uniformly hyperbolic infinite system follows the Liouvillian flow. This example supports the claim that a Gaussian wavepacket in a chaotic system follows the Liouvillian flow up to the timescale at which the wavepacket becomes so large that the Liouvillian dynamics ceases to be hyperbolic [34].

The uniformly hyperbolic Hamiltonian we consider is $\mathcal{H} = p_x^2/(2m) - m\lambda^2 x^2/2$. With the change of variable $p_x = (m\lambda/2)^{1/2}(q + p_q)$ and $x = (2m\lambda)^{-1/2}(q - p_q)$, the Hamiltonian can be written as

$$\mathcal{H} = \lambda (qp_q - i\hbar/2).$$

Solving the classical Hamilton equations of motion one gets $q(t) = q(0)e^{\lambda t}$ and $p_q(t) = p_q(0)e^{-\lambda t}$. Next, it is easily checked that a solution of the Schrödinger equation is provided by the wavepacket

$$\langle q|\psi(t)\rangle = A \exp[-\Delta^{-2}(t)[q - q(t) - i\Delta^2(t)p_q(t)/\hbar]^2],$$

with $\Delta(t) = \Delta(0)e^{\lambda t}$. Thus we see that a Gaussian wavepacket remains Gaussian, simply stretched and

shifted by the Liouvillian flow. This quantum calculation is exact if the system is infinite. In finite systems, initially narrow classical distributions undergo a crossover from hyperbolic dynamics to diffusive behavior once their extension become comparable to some characteristic length scale of the system [1]. In our case we can thus expect that Gaussian wavepackets cease to be Gaussian once the wavepacket has spread to a width of order the lead width. In other words a Gaussian wavepacket will remain Gaussian for times shorter than the Ehrenfest time [34].

APPENDIX B: ALGORITHMIC CONSTRUCTION OF AN ORTHOGONAL PHASE-SPACE BASIS

A basis of coherent states can be made complete (and not overcomplete) but not orthogonal, by placing coherent states at the vertices of a von Neumann lattice [49]. This complete basis can be orthogonalized by following standard procedures (e.g. Gram-Schmidt orthogonalization), upon which, however, the basis states become very different from one another and extended in phase-space. We here describe a numerical algorithm which orthogonalizes a complete basis of coherent states on a von Neumann lattice, keeping all states identical (up to a translation in phase space) while preserving the phase-space localization property of those states.

One starts from coherent states with wavefunctions

$$|\text{cs}; i, j\rangle = \exp\left[-\frac{1}{2}|\alpha_{ij}|^2\right] \exp[\alpha_{ij}\hat{a}^\dagger]|0\rangle. \quad (\text{B1})$$

The creation and annihilation operators are (here $\hbar = 1$)

$$\hat{a}^\dagger = 2^{-1/2}[\hat{Q} - i\hat{P}], \quad \hat{a} = 2^{-1/2}[\hat{Q} + i\hat{P}], \quad (\text{B2})$$

where $\alpha_{ij} = 2^{-1/2}[Q_i + iP_j]$ and using dimensionless position Q and momentum P with $[\hat{P}, \hat{Q}] = i$. The vacuum state, $|0\rangle$, is a Gaussian wavepacket centered at $P = Q = 0$,

$$\langle Q|0\rangle = \langle Q|\text{cs}; 0, 0\rangle = \pi^{-1/4} \exp[-\frac{1}{2}Q^2]. \quad (\text{B3})$$

The coherent state (B1) is a Gaussian wavepacket centered at $Q = Q_i$ and $P = P_j$ with the same spread in both directions,

$$\begin{aligned} \langle Q|\text{cs}; i, j\rangle &= \pi^{-1/4} \exp[iP_jQ - \frac{1}{2}[Q - Q_i]^2], \\ \langle P|\text{cs}; i, j\rangle &= \pi^{-1/4} \exp[-iPQ_i - \frac{1}{2}[P - P_i]^2], \end{aligned} \quad (\text{B4})$$

where we have dropped irrelevant overall phases.

To get a complete basis, coherent states are placed at each vertex but one of a square von Neumann lattice, i.e. a regular lattice on the Q - P plane with each unit cell covering an area (2π) [49]. Translational invariance means that the empty lattice vertex may be anywhere. This basis of coherent states is complete but it is not orthogonal. To orthogonalize it, we make the ansatz that there exists a set $\{\beta_i\}$ such that the wavefunction

$$|\text{ps}; i, j\rangle = \sum_{i', j'} \beta_{i'} \beta_{j'} |\text{cs}; i' + i, j' + j\rangle \quad (\text{B5})$$

obeys

$$\langle \text{ps}; k, l | \text{ps}; i, j \rangle = \delta_{ik} \delta_{jl}. \quad (\text{B6})$$

Note that the form of Eq. (B5) is such that we assume that the basis-states will be symmetric under interchange of Q and P just as the coherent states are.

To satisfy Eq. (B6), we see that the elements of the set $\{\beta_i\}$ must obey

$$\delta_{i,0} = \sum_{i' i''} \beta_{i'}^* \beta_{i''} \exp[-(\pi/2)(i + i' - i'')^2] \quad (\text{B7})$$

We define a set of vectors, $\{v^{(\alpha)}\}$, written in a non-orthogonal basis, $\{\hat{e}_i\}$, such that $v^{(\alpha)} = \sum_i \beta_{i-\alpha} \hat{e}_i$, i.e. the i th element of the α th basis vector is $v_i^{(\alpha)} = \beta_{i-\alpha}$. The basis is chosen such that the basis-vectors have the inner product $(\hat{e}_i \cdot \hat{e}_j) = \exp[-(\pi/2)(i - j)^2]$. The condition that the vectors $\{v^{(\alpha)}\}$ form an orthonormal basis is

$$\delta_{\alpha,0} = (v^{(\alpha)} \cdot v^{(0)}) = \sum_{ij} \beta_{i-\alpha}^* \beta_j (\hat{e}_i \cdot \hat{e}_j) \quad (\text{B8})$$

This is identical to the condition (B7), thus orthogonalizing this set of vectors is equivalent to finding the β 's which satisfy Eq. (B7). We use the following algorithm to orthogonalize these vectors

1. Take a complete normalized (but non-orthogonal) basis, $\{v_i\}$.
2. define a new basis such $\{v'_i\}$ such that $v'_i = A_i[v_i - \frac{1}{2} \sum_{j \neq i} (v_i \cdot v_j) v_j]$. We then choose A_i such that it normalizes the vector v'_i .
3. Repeat the procedure, taking the new basis $\{v'_i\}$ and deriving a basis $\{v''_i\}$, and so on.

We take the coherent states described above as the initial non-orthogonal basis, so initially $\beta_i = \delta_{i,0}$. In Table I we present data for the first ten iterations of the algorithm, by the sixth iteration the results satisfy Eq. (B7) with an accuracy of $\lesssim 10^{-7}$. Each iteration improves the accuracy by more than one order of magnitude. A PS-state generated by this procedure is shown in Fig. 6. We note that β_i decays approximately exponentially with i . Thus the PS-states given by Eq. (B5) are exponentially localized in position and momentum, as shown in Fig. 6.

Area-preserving stretches, $(Q, P, Q_j, P_j) \rightarrow (\kappa Q, \kappa^{-1}P, \kappa Q_j, \kappa^{-1}P_j)$, and rotations $(Q, P, Q_j, P_j) \rightarrow (Q \cos \theta + P \sin \theta, P \cos \theta - Q \sin \theta, Q_j \cos \theta + P_j \sin \theta, P_j \cos \theta - Q_j \sin \theta)$ are unitary operation for any κ, θ . Thus the stretched-rotated basis will also be orthonormal and complete. This legitimizes the procedure discussed in Section IIIB for optimizing the PS-basis by fitting it to the PS scattering band structure.

Iterations	β_0	β_1	β_2	β_3	β_4	β_5	β_6	β_7	β_8	β_9	β_{10}
0	1	0	0	0	0	0	0	0	0	0	0
2	1.0386424	-0.1137192	1.93720E-2	-3.0781E-3	5.24E-6	4.3E-6	~ 0	~ 0	~ 0	~ 0	~ 0
4	1.0357044	-0.1130793	1.74448E-2	-3.0142E-3	5.478E-4	-1.024E-4	1.95E-5	-3.8E-6	7E-7	-1E-7	~ 0
6	1.0357044	-0.1130793	1.74448E-2	-3.0142E-3	5.478E-4	-1.024E-4	1.95E-5	-3.8E-6	7E-7	-1E-7	~ 0
10	1.0357044	-0.1130793	1.74448E-2	-3.0142E-3	5.478E-4	-1.024E-4	1.95E-5	-3.8E-6	7E-7	-1E-7	~ 0

TABLE I: Iterations of the orthogonalization algorithm for coherent states on a von Neumann grid. The table shows the value of $\beta_i = \beta_{-i}$ as the algorithm is iterated ($\beta_j \sim 0$ means that $|\beta_j| < 10^{-7}$). The algorithm converges with accuracy 10^{-7} after six iterations. Arbitrary large accuracies are obtained with more iterations. The PS-states are found by substituting the tabulated values into Eq. (B5).

APPENDIX C: EDGE-OF-BAND PHASE-SPACE STATES

The tails of the PS-state shown in Fig. 6 decays exponentially with the number of lattice points away from the center of the PS-state. Strictly speaking, any PS-state has thus a finite amplitude outside the band. We can however treat PS-states as classical, i.e. completely inside one band, if they are more than j_{\max} lattice sites away from the edge of that band. If we choose $j_{\max} = 1$, we would call states “classical” even if they have $\sim 3\%$ of their squared amplitudes outside the band (this is similar to the situation sketched in Fig. 7). If however we take $j_{\max} = 3$, then a PS-state is only classical if less than 10^{-5} of its squared amplitude is outside the band. The number of edge-of-band states (PS-states that are partially inside, partially outside a band with area $> 2\pi\hbar_{\text{eff}}$) of a band which exits at time τ is

$$n_{\text{eob}}^{L \rightarrow K}(\tau) \simeq 4j_{\max} \left(\frac{W_L W_K}{2\pi\hbar_{\text{eff}} L^2} \right)^{1/2} \exp[-\lambda\tau/2], \quad (\text{C1})$$

where $K = L, R$. Thus the number of edge-of-bands states is

$$N_{\text{eob}} = \sum_K \int_0^{\tau_E^{LK}} d\tau \mathcal{N}_{\text{band}}^{L \rightarrow K}(\tau) n_{\text{eob}}^{L \rightarrow K}(\tau) \sim \frac{j_{\max} N_{\text{qm}}}{\lambda\tau_D} \quad (\text{C2})$$

where the sum is over $K = L, R$ and j_{\max} is a number of order one. Note that the error we make decays exponentially with j_{\max} , hence the choice of acceptable error only changes N_{eob} logarithmically. From Eq. (C2) we conclude that the edge-of-band PS-states are a subdominant proportion of the total number of quantum PS-states, and can be ignored.

APPENDIX D: FLUX ENCLOSED BY THE CORRELATED PART OF THE LOOP

Here we analyze the part of the area enclosed by a loop-forming trajectory when it is in the correlation region

close to the crossing, i.e. within $T_L(\epsilon/2)$ of the crossing. The situation is depicted in Fig. 15. We consider a loop formed after N bounces at the cavity’s wall. In the correlation region, the segment of the trajectory between the

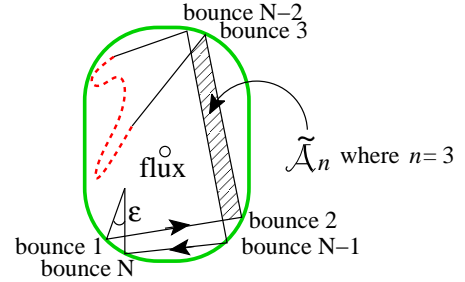


FIG. 15: A sketch of the area enclosed by the correlated part of the weak localization loop. The area $\tilde{\mathcal{A}}_n$ is defined by the segment of the loop-forming trajectory between the $(n-1)$ th and n th collisions and the segment between the $(N-n+1)$ th and the $(N-n+2)$ th collisions. (dashed region).

$(n-1)$ th and n th collision with the cavity walls, is highly correlated with the segment between the $(N-n+1)$ th and the $(N-n+2)$ th collision. We consider the directed area $\tilde{\mathcal{A}}_n$ enclosed by these two segments (dashed region in Fig. 15). We assume that $|\tilde{\mathcal{A}}_n|$ is uncorrelated with $|\tilde{\mathcal{A}}_{m \neq n}|$, and take each such area from a Gaussian distribution. The typical perpendicular distance between the trajectories at time t (measured from the crossing) is $\pm v_F \epsilon \lambda^{-1} \sinh(\lambda n \tau_0)$. Thus we assume $\langle \tilde{\mathcal{A}}_n \rangle = 0$ and

$$\langle \tilde{\mathcal{A}}_n^2 \rangle = \left[v_F^2 \epsilon \lambda^{-1} \int_{(n-1)\tau_0}^{n\tau_0} dt \sinh(\lambda t) \right]^2. \quad (\text{D1})$$

This grows exponentially with n . Thus the sum over the $\tilde{\mathcal{A}}_n$ ’s is dominated by the largest of them with $n_{\max} = T_L(\epsilon)/2\tau_f$, whose variance is $\sim A^2$. Anticorrelations in the signs of consecutive directed areas in the correlated region further reduce the total directed area. The flux enclosed in the correlated region is thus at most $\simeq A^2 \Phi^2$. This is smaller than the flux enclosed in the uncorrelated region by a factor $\tau_f/\tau_D \ll 1$.

-
- [1] A.J. Lichtenberg and M.A. Liebermann, *Regular and Chaotic Dynamics*, (Springer, Berlin, 1983).
- [2] J.-P. Eckmann and D. Ruelle, *Rev. Mod. Phys.* **57**, 617 (1985).
- [3] L. Wirtz, J.-Z. Tang, and J. Burgdörfer, *Phys. Rev. B* **59**, 2956 (1999); this paper discusses scattering bands in the context of quantum transport in a chaotic billiard, but it does not make the connection between their area and the quantum phase-space resolution \hbar_{eff} .
- [4] P.G. Silvestrov, M.C. Goorden, and C.W.J. Beenakker, *Phys. Rev. B* **67**, 241301(R) (2003).
- [5] J. Tworzydło, A. Tajic, H. Schomerus and C.W.J. Beenakker, *Phys. Rev. B* **68**, 115313 (2003).
- [6] J. Tworzydło, A. Tajic and C.W.J. Beenakker, *Phys. Rev. B* **69**, 165318 (2004).
- [7] Ph. Jacquod, and E.V. Sukhorukov, *Phys. Rev. Lett.* **92**, 116801 (2004).
- [8] M.C. Goorden, Ph. Jacquod, and C.W.J. Beenakker, *Phys. Rev. B* **72**, 064526 (2005).
- [9] The dwell time is exactly the same for all trajectories within a band for maps such as the kicked rotator used in Figs. 1 and 3.
- [10] L.P. Kouwenhoven, C.M. Marcus, P.L. McEuen, S. Tarucha, R.M. Westervelt, and N.S. Wingreen, *Electron Transport in Quantum Dots*, Nato ASI conference proceedings, L.P. Kouwenhoven, G. Schön, and L.L. Sohn Eds. (Kluwer, Dordrecht, 1997); Y. Alhassid, *Rev. Mod. Phys.* **72**, 895 (2000); I.L. Aleiner, P.W. Brouwer, and L.I. Glazman, *Phys. Rep.* **358**, 309 (2002).
- [11] H.U. Baranger, R.A. Jalabert, and A.D. Stone, *Chaos* **3**, 665 (1993).
- [12] C.M. Marcus, R.M. Westervelt, P.F. Hopkins, and A.C. Gossard, *Chaos* **3**, 643 (1993).
- [13] M. L. Mehta, *Random Matrices* (academic, New York, 1991).
- [14] R.A. Jalabert, J.-L. Pichard, and C.W.J. Beenakker, *Europhys. Lett.* **27**, 255 (1994); H.U. Baranger and P.A. Mello, *Phys. Rev. Lett.* **73**, 142 (1994).
- [15] S. Heusler, S. Müller, P. Braun, and F. Haake, *Phys. Rev. Lett.* **96**, 066804 (2006).
- [16] G.P. Berman and G.M. Zaslavsky, *Physica A* **91**, 450 (1978).
- [17] S. Oberholzer, E.V. Sukhorukov, and C. Schönenberger, *Nature (London)* **415**, 765 (2002).
- [18] Ya.M. Blanter and M. Büttiker, *Phys. Rep.* **336**, 1 (2000).
- [19] C.W.J. Beenakker and H. van Houten, *Phys. Rev. B* **43**, R12066 (1991); the semiclassical limit requires that one adapts the voltage in order to fix the injection rate of electrons, so $V \propto N_L^{-1}$ as $\hbar_{\text{eff}} \rightarrow 0$. If the voltage were fixed, the shot-noise power would diverge as $\hbar_{\text{eff}} \rightarrow 0$. We thank Carlo Beenakker for a discussion of this point.
- [20] O. Agam, I. Aleiner and A. Larkin, *Phys. Rev. Lett.* **85**, 3153 (2000).
- [21] R.S. Whitney and Ph. Jacquod, *cond-mat/0512516*.
- [22] R.S. Whitney, and Ph. Jacquod, *Phys. Rev. Lett.* **94**, 116801 (2005).
- [23] For a recent review on the quantum-to-classical correspondence in open systems see: H. Schomerus and Ph. Jacquod, *J. Phys. A* **38**, 10663 (2005).
- [24] I.L. Aleiner and A.I. Larkin, *Phys. Rev. B* **54**, 14423 (1996).
- [25] İ. Adagideli, *Phys. Rev. B* **68**, 233308 (2003).
- [26] J. Tworzydło, A. Tajic and C.W.J. Beenakker, *Phys. Rev. B* **70**, 205324 (2004).
- [27] S. Rahav and P.W. Brouwer, *Phys. Rev. Lett.* **95**, 056806 (2005); *cond-mat/0507035*.
- [28] M.G. Vavilov and A.I. Larkin, *Phys. Rev. B* **67**, 115335 (2003).
- [29] W. Bauer and G.F. Bertsch, *Phys. Rev. Lett.* **65**, 2213 (1990).
- [30] H. Schomerus and J. Tworzydło, *Phys. Rev. Lett.* **93**, 154102 (2004).
- [31] I. Daubechie, *Ten Lectures on Wavelets* (SIAM, Philadelphia, 1992); G. Kaiser, *A Friendly Guide to Wavelets* (Birkhäuser, Boston, 1994).
- [32] If the L lead is covered with PS-states placed on a square grid, then each PS-state has a spread of $\hbar_{\text{eff}}^{1/2}$ in r and p . Thus a classical band which is narrower than $\hbar_{\text{eff}}^{1/2}$ could not contain any PS-states, despite the band's phase-space area being $\sim \hbar_{\text{eff}}^{1/2} W/L \gg \hbar_{\text{eff}}$. This would lead to the prediction that the open cavity Ehrenfest time is $\lambda^{-1} \ln[\hbar_{\text{eff}}^{1/2} W/L]$ (for $W_L = W_R = W$), which is half the value found by using the optimized PS-basis, see Eq. (8).
- [33] In Eq. (11), λ is, strictly speaking, not the Lyapunov exponent, but rather the local rate of stretching of the Liouvillian flow averaged along the given trajectory. This distinction is important for the covering of non-parallelogram bands.
- [34] E.J. Heller and S. Tomsovic, *Phys. Today* **46**(7), 38 (1993).
- [35] D.S. Fisher and P.A. Lee, *Phys. Rev. B* **23**, R6851 (1981).
- [36] For an ideal lead, with N lead modes of the form $\langle y|n \rangle = (2/W)^{1/2} \sin(\pi y n/W)$ for $0 \leq y \leq W$, one finds that $\sum_n \langle y'|n \rangle \langle n|y \rangle = (2W)^{-1} [\sin[(z' - z)(N + 1/2)] / \sin[(z' - z)/2] - \sin[(z' + z)(N + 1/2)] / \sin[(z' + z)/2]]$ where $z = \pi y/W$. This function is strongly peaked at $y' = y$ with peak width $\sim \lambda_F$ and height $\sim \lambda_F^{-1}$, in the semiclassical limit we can calculate all quantities to lowest order in \hbar by approximating this function with a Dirac δ -function.
- [37] K. Richter and M. Sieber, *Phys. Rev. Lett.* **89**, 206801 (2002).
- [38] M. Sieber and K. Richter, *Phys. Scr.* **T90**, 128 (2001).
- [39] Unlike in Section II B, we neglect the lead asymmetry in the definition of $T_W(\epsilon)$, which would lead to corrections of order $\sim \ln|W_L/W_R|$ only. Neglecting them is consistent with our treatment of weak localization which neglects other corrections of order one inside logarithms of the Ehrenfest and ϵ -times. See the remark before Eq. (45).
- [40] This is the origin of our incorrect previous prediction that g_{wl} would not decay with τ_E^{cl} [22]. Our reasoning was that the probability to return should be the inverse volume of the quantum phase-space rather than the total phase-space. That reasoning is incorrect, as shown by the present calculation where crossings contributions are clearly identified. Here, one is left with probabilities for classical trajectories which know nothing of \hbar or τ_E^{cl} . The suppression we expected due to the existence of bands is fully accounted for in the correlated escape probabilities for almost parallel trajectories within W of each other, it reduces the decay from $\exp[-(\tau_E^{\text{cl}} + \tau_E^{\text{op}})/\tau_D]$ to

- $\exp[-\tau_E^{\text{cl}}/\tau_D]$.
- [41] F. M. Izrailev, Phys. Rep. **196**, 299 (1990).
 - [42] J.H. Bardarson, J. Tworzydło, and C.W.J. Beenakker, Phys. Rev. B **72**, 235305 (2005).
 - [43] Y.V. Fyodorov and H.-J. Sommers, JETP Letters **72**, 422 (2000); R.O. Vallejos and A.M. Ozorio de Almeida, Ann. Phys. **278**, 86 (1999).
 - [44] Our semiclassics implicitly averages over encounters distributed all over phase-space. The exponential suppression of weak localization is thus $\propto \langle \exp[-\tau_E^{\text{cl}}/\tau_D] \rangle$. For systems which are nonuniformly hyperbolic such as the kicked rotator, the “Lyapunov exponent” measured by the decay of weak-localization might thus differ from $\ln[K/2] = \langle \lambda \rangle$. A similar effect has been found in the decay of the fidelity in dynamical systems, P.G. Silvestrov, J. Tworzydło, and C.W.J. Beenakker, Phys. Rev. E **67**, 025204(R) (2003); C. Petitjean and Ph. Jacquod, Phys. Rev. E **71**, 036223 (2005).
 - [45] P. Marconcini, M. Macucci, G. Iannaccone, B. Pellegrini, and G. Marola, Europhys. Lett. **73**, 574 (2006).
 - [46] F. Aigner, S. Rotter, and J. Burgdörfer, Phys. Rev. Lett. **94**, 216801 (2005).
 - [47] A.M. Chang, H.U. Baranger, L.N. Pfeiffer, and K.W. West, Phys. Rev. Lett. **73**, 2111 (1994).
 - [48] S. Rahav and P.W. Brouwer, Phys. Rev. Lett. **96**, 196804 (2006).
 - [49] A. Perelomov, *Generalized Coherent States and Their Application*, (Springer-Verlag, Berlin, 1986).